

# 1 Robot-Accelerated Perovskite Investigation and Discovery

2 Zhi Li, Mansoor Ani Najeeb, Liana Alves, Alyssa Z. Sherman, Venkateswaran Shekar, Peter Cruz Parrilla,  
 3 Ian M. Pendleton, Wesley Wang, Philip W. Nega, Matthias Zeller, Joshua Schrier,\*  
 4 Alexander J. Norquist,\* and Emory M. Chan\*



Cite This: <https://dx.doi.org/10.1021/acs.chemmater.0c01153>



Read Online

ACCESS |

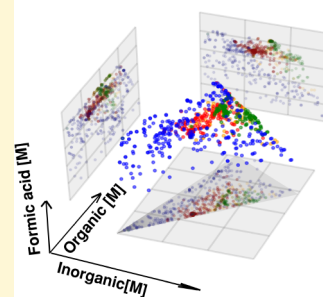
Metrics & More

Article Recommendations

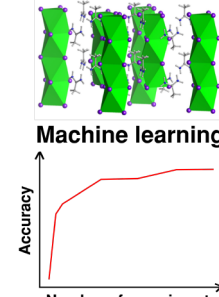
Supporting Information

5 **ABSTRACT:** Metal halide perovskites are a promising class of materials  
 6 for next-generation photovoltaic and optoelectronic devices. The  
 7 discovery and full characterization of new perovskite-derived materials  
 8 are limited by the difficulty of growing high quality crystals needed for  
 9 single-crystal X-ray diffraction studies. We present an automated, high-  
 10 throughput approach for metal halide perovskite single crystal discovery  
 11 based on inverse temperature crystallization (ITC) as a means to rapidly  
 12 identify and optimize synthesis conditions for the formation of high  
 13 quality single crystals. Using this automated approach, a total of 8172  
 14 metal halide perovskite synthesis reactions were conducted using 45  
 15 organic ammonium cations. This robotic screening increased the number  
 16 of metal halide perovskite materials accessible by an ITC synthesis route  
 17 by more than 5-fold and resulted in the formation of two new phases,  
 18  $[C_2H_7N_2][PbI_3]$  and  $[C_7H_{16}N]_2[PbI_4]$ . This comprehensive data set allows for a statistical quantification of the total experimental  
 19 space and of the likelihood of large single crystal formation. Moreover, this data set enables the construction and evaluation of  
 20 machine learning models for predicting crystal formation conditions. This work is a proof-of-concept that combining high  
 21 throughput experimentation and machine learning accelerates and enhances the study of metal halide perovskite crystallization. This  
 22 approach is designed to be generalizable to different synthetic routes for the acceleration of materials discovery.

## Robot-accelerated synthesis



## New perovskites



## 23 ■ INTRODUCTION

24 Metal halide perovskites<sup>1,2</sup> can exhibit tunable electronic  
 25 properties<sup>3–6</sup> that are leveraged in optoelectronic,<sup>7–11</sup> thermo-  
 26 electric,<sup>12,13</sup> and photovoltaic devices,<sup>14–19</sup> for which power  
 27 conversion efficiencies of 24.2% have been achieved.<sup>20</sup> The  
 28 composition and structure of metal halide perovskites  
 29 determine electronic properties such as carrier mobilities and  
 30 band structure.<sup>6,21</sup> However, access to suitable crystalline  
 31 perovskites for detailed characterization of their structure and  
 32 physical properties has been hindered by limited under-  
 33 standing of the underlying processes through which large high  
 34 quality single crystals grow.

35 A diverse array of synthetic routes exist for the growth of  
 36 metal halide perovskite single crystals, including antisolvent  
 37 vapor-assisted crystallization,<sup>22–25</sup> seeded crystal growth,<sup>26,27</sup>  
 38 slow evaporation,<sup>28,29</sup> and inverse temperature crystallization  
 39 (ITC).<sup>30–33</sup> ITC is a promising choice for structural studies of  
 40 new perovskite materials because it can be used to grow high  
 41 quality crystals without the need for long growth times. To  
 42 date, metal halide perovskite ITC behavior, in which the  
 43 solubility decreases with increased temperature, has been  
 44 observed for only four compositions: methylammonium lead  
 45 iodide ( $MAPbI_3$ ), methylammonium lead bromide  
 46 ( $MAPbBr_3$ ), formamidinium lead iodide ( $FAPbI_3$ ), and  
 47 formamidinium lead bromide ( $FAPbBr_3$ ).<sup>34–36</sup> Extension of

the ITC route to new chemical systems is slow because 48  
 successful crystal growth using this technique requires the 49  
 simultaneous optimization of a large number of interdependent 50  
 parameters such as reagent concentration and reaction 51  
 temperature, necessitating many experimental trials. 52

High-throughput synthetic approaches are well-suited for 53  
 efficiently exploring large experimental parameter spaces.<sup>37</sup> 54  
 Such approaches have been used to search for new organic 55  
 reactions,<sup>38–41</sup> optimize synthetic conditions of inorganic 56  
 materials,<sup>42–45</sup> and discover new inorganic materials for 57  
 energy, catalysis, and sensing applications.<sup>46–52</sup> Specifically, 58  
 high-throughput approaches have been used to explore the 59  
 formation of metal halide perovskites in the form of thin- 60  
 films,<sup>53,54</sup> polycrystalline samples,<sup>50</sup> nanocrystals,<sup>55,56</sup> and, 61  
 recently, as single crystals produced by antisolvent vapor- 62  
 assisted crystallization.<sup>52</sup> The application of such high- 63  
 throughput approaches to the growth of metal halide 64

Received: March 17, 2020

Revised: June 4, 2020

Published: June 4, 2020

65 perovskite single crystals requires the adaptation of exper-  
66 imental routes to ensure compatibility with liquid handling  
67 robotics. Optimal utilization of high-throughput data sets  
68 requires the capture of nuanced experimental details that  
69 enable subsequent analysis with machine learning models,  
70 which have shown promise in this domain.<sup>52–55,57–63</sup>

71 In this report, we describe a series of high-throughput metal  
72 halide perovskite crystal growth experiments, using a new  
73 platform for Robot-Accelerated Perovskite Investigation and  
74 Discovery (RAPID). A total of 8172 individual crystallization  
75 reactions were performed via ITC across 45 chemical systems.  
76 This RAPID screening increased the number of metal halide  
77 perovskite systems for which ITC conditions can be used to  
78 grow crystals by more than 5-fold. Additionally, our work  
79 resulted in the discovery of two new compounds,  $C_2H_7N_2PbI_3$   
80 and  $(C_7H_{16}N)_2PbI_4$ . Experiment generation and data manage-  
81 ment in the high throughput workflow were enabled by a  
82 software pipeline, ESCALATE (Experiment Specification,  
83 Capture and Laboratory Automation Technology),<sup>64</sup> to both  
84 capture a complete record of the high-throughput experiments  
85 and observational data, and to format those data for use in  
86 machine learning studies. The resulting data set was used to  
87 train machine learning models for each chemical system,  
88 demonstrating the utility of our high-throughput approaches to  
89 metal halide perovskite crystal growth.

## 90 ■ RESULTS AND DISCUSSION

91 **Robot Accelerated Perovskite Workflow.** A high-  
92 throughput robotic synthesis of perovskites imposes three  
93 practical constraints. First, the use of a liquid handling robot  
94 necessitates that all reagents be dispensed as homogeneous  
95 solutions. The solubilities of the reactive species thus define  
96 the upper bounds of the chemical concentration space in which  
97 reactions can be performed, while the lower bounds are  
98 necessarily zero (i.e., solvent only). If data are to be used for  
99 subsequent modeling, then software such as ESCALATE<sup>64</sup>  
100 must capture all of these experimental details, even for manual  
101 operations such as the preparation of stock solutions. Second,  
102 chemical compatibility with the robot precludes the use of  
103 strong acids, such as HI. Only weak acids, such as formic acid,  
104 are allowed in the experiment to avoid robot damage. Third,  
105 heating block limitations, as well as the flash point of solvents,  
106 constrain reaction temperatures from 95 °C to room  
107 temperature. We classify any synthesis satisfying these  
108 constraints as “RAPID”.

109 In this paper, we describe a RAPID ITC route for the  
110 formation of metal halide perovskite single crystals. The  
111 solubilities of all reactants are measured (see Table S2 in the  
112 Supporting Information, SI) to ensure that stock solutions  
113 utilize the highest possible concentrations of the dissolved  
114 species, maximizing the amount of chemical space available for  
115 exploration. The liquid handling robot pipets four different  
116 types of stock solutions into 96 well microplates: (1) a stock  
117 solution of lead(II) halide and the selected organoammonium  
118 halide, included to increase the solubility of the lead halide; (2)  
119 a stock solution of the selected organoammonium halide; (3)  
120 pure solvent; and (4) neat formic acid. The stock solutions are  
121 prepared in one of three solvents:  $\gamma$ -butyrolactone (GBL),  
122 dimethyl sulfoxide (DMSO), and dimethylformamide (DMF)  
123 (see Table S2 for the solvent used in each chemical system).  
124 After dispensing the reagent solutions, the liquid handler  
125 vortexes and heats the microplates to ensure that the solutions  
126 are fully mixed. After vortexing is complete, the resulting

127 perovskite solutions are heated undisturbed for 2.5 h to allow  
128 for crystal growth. An experimental flowchart describing  
129 reagent selection, benchtop testing, reaction components,  
130 stock solution preparation, and robotic reaction is shown in  
131 Figure S4. All variables with explanation of their bounds and  
132 values in the experiments are specified in Table S3, and  
133 detailed experimental procedures are available in the SI. Initial  
134 experiments focused on  $Pb^{2+}$  and  $I^-$ , the most explored metal  
135 and halide combination in metal halide perovskites. Iodides are  
136 generally more stable than chlorides and bromides and have  
137 narrower band gaps more appropriate for solar applications.<sup>5,65</sup>  
138 Using formic acid promotes crystallization by shifting the lead  
139 iodide equilibrium from colloidal cluster species to ionic  
140 species, reducing the crystallization onset temperature.<sup>30,66</sup>  
141 Formic acid is a sufficiently weak acid to be compatible with  
142 the NIMBUS liquid handling robot used in this work.  
142

The selection of specific reactant concentrations, with  
143 corresponding solution volumes, is performed using a quasi-  
144 random sample of the possible experimental composition  
145 parameters through ESCALATE.<sup>64</sup> Additionally, ESCALATE  
146 generates complete sets of instructions for the human  
147 operators (e.g., stock solution preparation) and the input  
148 files used by the robot to perform the experiments.  
149 ESCALATE is then used to capture the complete set of  
150 operator actions, ambient conditions, operator observations,  
151 and instrument log files associated with each reaction, along  
152 with relevant metadata.<sup>64</sup> Although the experiment generation  
153 and data management processes could have been performed  
154 manually, ESCALATE automated and accelerated these  
155 processes to meet the requirements for high-throughput  
156 experimentation. Among the observational data is a visual  
157 score of crystallite size for each reaction vial, following the  
158 scheme of our previous work and that of Cooper and co-  
159 workers.<sup>60,67</sup> Photographs of reaction vials are captured and  
160 reaction outcomes are scored into four classes: (1) clear  
161 solution without any solid; (2) fine powder; (3) small  
162 crystallites (average crystal dimension <0.1 mm); and (4)  
163 large (>0.1 mm) crystals suitable for structure determination  
164 by single crystal X-ray diffraction (see Crystal Scoring Rubric  
165 in the SI and examples of crystal images and their scores in  
166 Table S1 and Figure S2). The entire life-cycle of an experiment  
167 is shown in Figure S3. The complete data set from these  
168 reactions, including outcomes, crystal images, X-ray diffraction  
169 patterns, and modeling, is accessible via the SI; these data can  
170 be analyzed and visualized interactively using the online scripts  
171 provided<sup>68</sup> (see Interactive Data Visualization and Analysis  
172 Interface section in the SI). Detailed descriptions of the  
173 experimental and computed features used for this work are  
174 provided in the SI. Crystallization outcomes, and the features  
175 of the experiments that produced them, are tabulated in a  
176 comma-separated-value (CSV) file publicly available at  
177 <https://github.com/darkreactions/rapid>.<sup>69</sup>  
178

**High-Throughput Screening.** A total of 8172 ITC  
179 reactions were performed in 45 different chemical systems,  
180 each of which contains lead(II) iodide and an organic cation.  
181 Here, 45 structurally diverse organoammoniums are chosen as  
182 organic cations, including aliphatic ammonium ions [e.g.,  
183 methylammonium (MA), ethylammonium (EtA)]; aromatic  
184 cations [e.g., phenethylammonium (PhenEtA), benzylammo-  
185 nium (BenA)]; linear chains [e.g., *n*-butylammonium (*n*BuA),  
186 *n*-dodecylammonium (*n*DodA)]; branched structures [e.g.,  
187 iso-butylammonium (iBuA), acetamidinium (Acet)]; cyclic  
188 cations [e.g., cyclohexylammonium (CHA)]; secondary and  
189

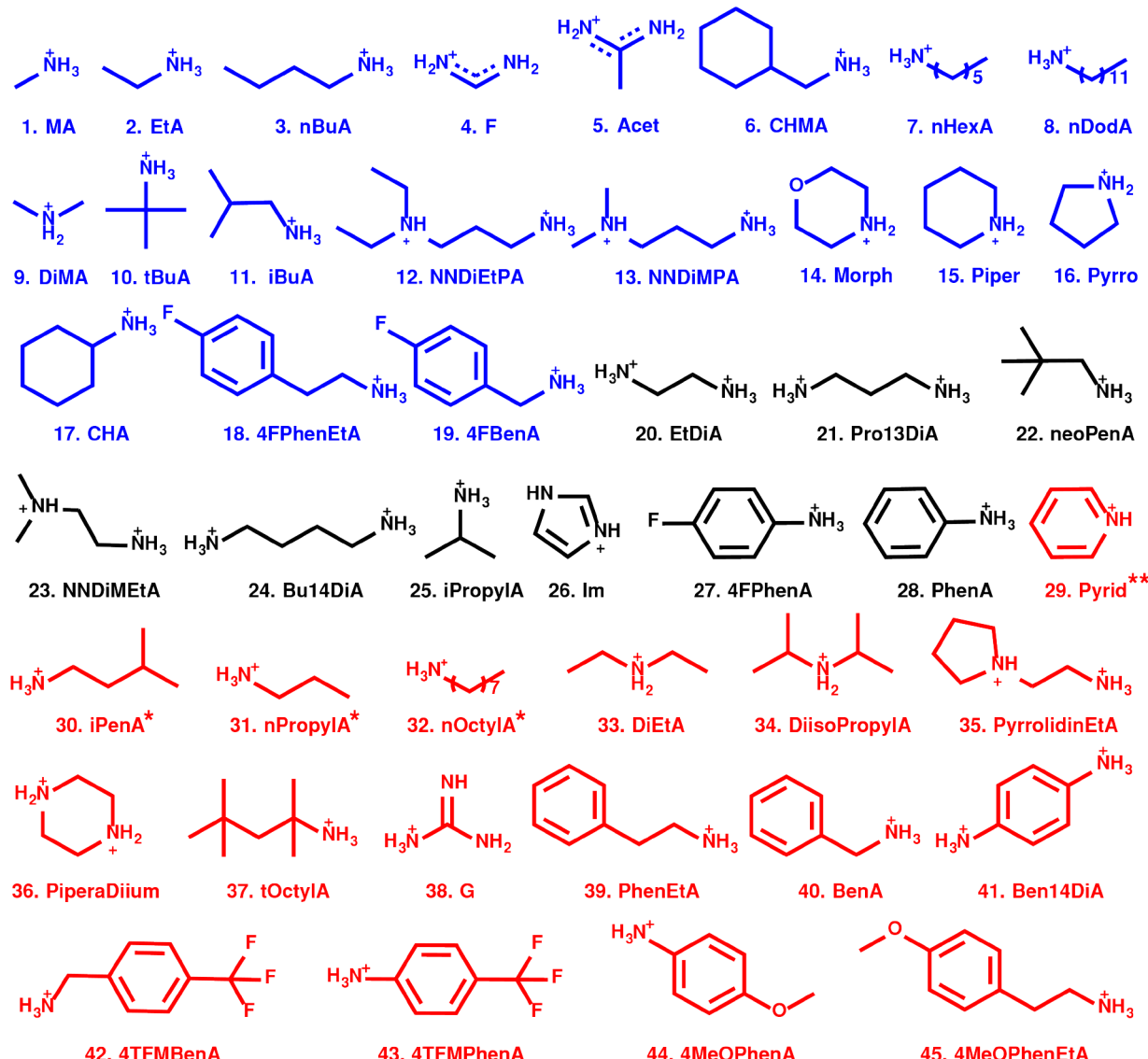


**Figure 1.** Chemical structures of the organoammonium cations studied in this work (see Table S2 for full chemical names). Blue-colored structures produce Class 4 large crystals confirmed to be perovskite-derived phases. Black structures produce Class 4 crystals with unknown structure (i.e., powder-XRD patterns do not match any known phases of perovskite-derived compounds,  $\text{PbI}_2$ , or organoammonium iodides). Red-colored cations produce only Class 1–3 outcomes or  $\text{PbI}_2$  crystals. Single asterisk (\*) indicates cations producing Class 3 outcomes with unknown phase. Double asterisk (\*\*) indicates Class 3 outcomes confirmed as a perovskite-derived phase.

190 tertiary ammoniums [e.g.,  $N,N$ -diethylpropane-1,3-diammonium 191 nium (NNDiEtPA)]; and amidinium ions [e.g., formamidinium 192 nium (FA)]. Chemical structures and abbreviations for these 193 45 organoammoniums are shown in Figure 1. These 194 compounds comprise all of the organoammonium iodides 195 sold by the vendor (GreatCell Inc.), providing a survey of the 196 most accessible region of chemical space and the one most 197 replicable by other chemists. Reactions within a given system 198 vary in their lead iodide, organoammonium iodide and formic 199 acid concentrations. As shown in Figures 2, S5, and S6, high- 200 throughput screening allowed for the identification of 201 conditions that result in large crystals (indicated by red 202 circles) for each chemical system, demonstrating the efficacy of 203 exploratory work using this automated workflow. Whereas only 204 methylammonium (MA) and formamidinium (F) halide 205 perovskites were previously known to form via ITC,<sup>34–36</sup> we 206 find that ITC is possible for perovskites that incorporate 207 organoammonium cations with a much wider range of 208

molecular weights, degree of ammonium substitution, and 209 structural features such as aliphatic and aromatic rings. The 210 high-throughput screening results for all 45 chemical systems 211 are accessible through our interactive data visualization and 212 analysis interface (For example images, see Figure S1).<sup>68</sup>

The conditions for which large, macroscopic crystals grow 213 often cluster in a single region of chemical concentration space 214 for each chemical system, with cluster positions varying 215 between systems. For the synthesis of  $\text{EtAPbI}_3$  at 95 °C 216 (Figure 2b), large, Class 4 crystals are formed in the 217 intermediate inorganic and organic concentration regime 218 (0.3–0.8 M and 1–2 M, respectively) with a high 219 concentration of formic acid (>6.0 M). Higher lead iodide 220 concentrations tend to produce fine powders (Class 2) because 221 such high  $\text{PbI}_2$  concentrations induce faster nucleation. 222 Conversely, lower concentrations of lead iodide do not result 223 in any solid product.<sup>15</sup> The observation that adding formic acid 224 facilitates crystallization is consistent with reports by Snaith 225

- Class 4: Large crystals
- Class 3: Small crystallites
- Class 2: Fine powder
- Class 1: Clear solution

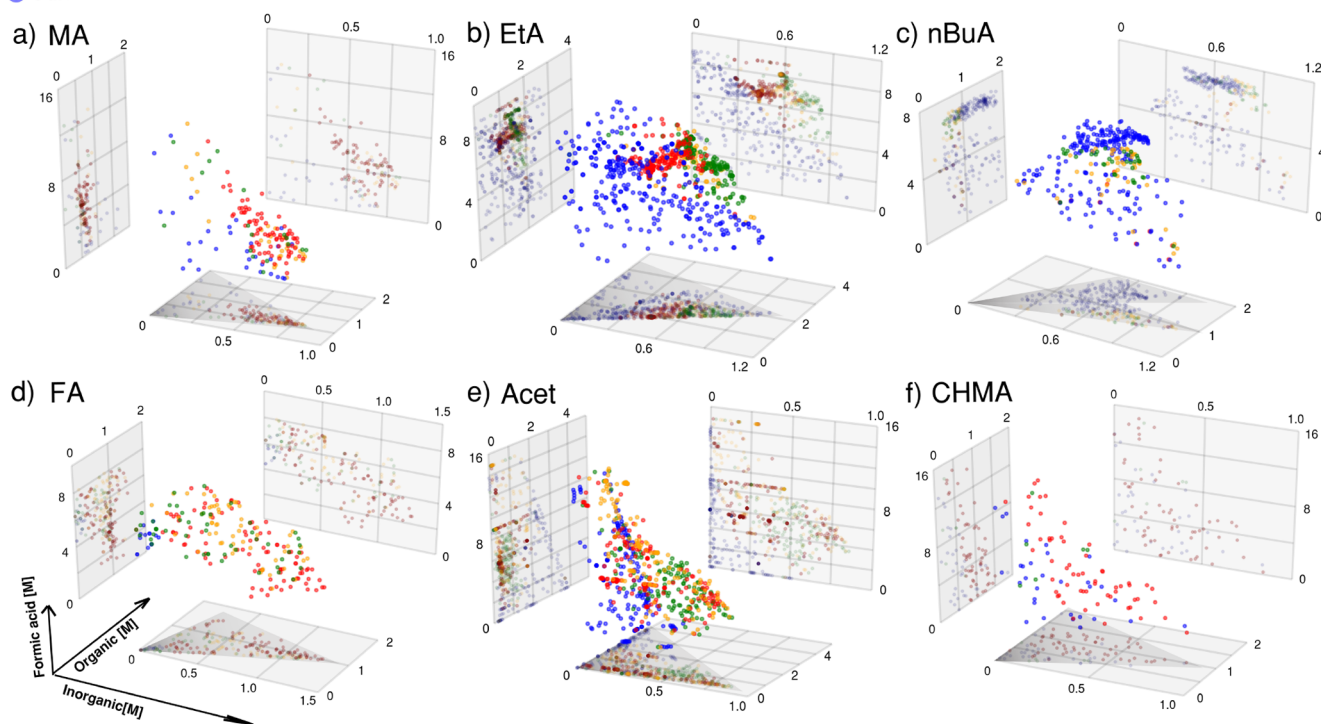


**Figure 2.** Crystal quality of 2295 lead iodide perovskite reactions as a function of the organic cation and the concentrations of the organic, inorganic ( $\text{PbI}_2$ ), and formic acid precursors. Organic precursors are methylammonium iodide (a), ethylammonium iodide (b), *n*-butylammonium iodide (c), formamidinium iodide (d), acetamidinium iodide (e), and cyclohexylmethylammonium iodide (f). Reactions shown were performed at 95 °C. Light gray boxes show two-dimensional projections of the data. Dark gray triangles illustrate the accessible experimental space in the organic–inorganic plane, as constrained by precursor solubilities. Additional data for other organoammonium precursors are shown in Figures S5 and S6 and in the interactive data visualization interface.<sup>68</sup>

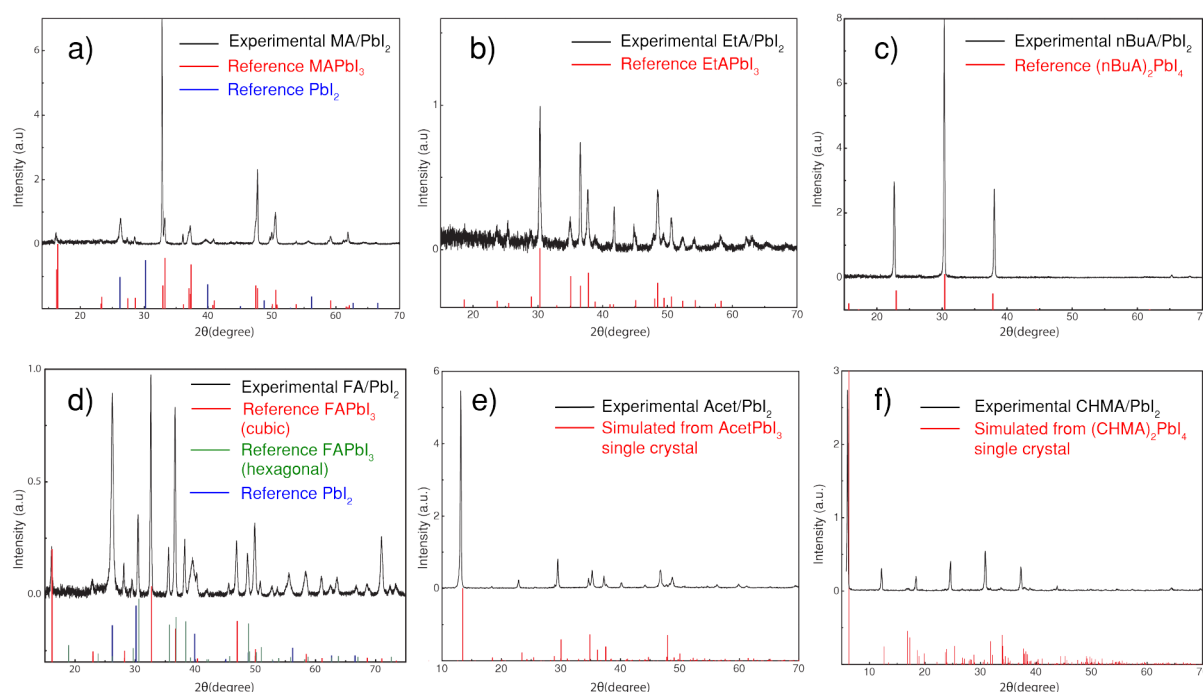


**Figure 3.** Powder X-ray diffraction patterns of crystals grown from the following systems: MA/PbI<sub>2</sub> (a), EtA/PbI<sub>2</sub> (b), nBuA/PbI<sub>2</sub> (c), FA/PbI<sub>2</sub> (d), Acet/PbI<sub>2</sub> (e), and CHMA/PbI<sub>2</sub> (f). See text for ICSD numbers for reference patterns.

226 and co-workers;<sup>70</sup> increasing the acidity of the reaction  
227 solution dissolves  $\text{PbI}_x$  colloid intermediates, raising the  
228 effective lead and iodide concentrations, and in turn promoting  
229 metal halide perovskite single crystal formation.

230 Powder X-ray diffraction measurements (pXRD) performed  
231 on ground, Class 4 samples from RAPID reactions indicate  
232 that tetragonal  $\text{MAPbI}_3$ <sup>30,71</sup> was successfully synthesized from  
233 the MA/PbI<sub>2</sub> reaction system (Figure 3a). The FA/PbI<sub>2</sub>  
234 system predominantly produced cubic FAPbI<sub>3</sub> mixed with  
235 the hexagonal phase (Figure 3d), which is not surprising in  
236 light of the bistability of this compound and its propensity  
237 toward phase transitions.<sup>72,73</sup> Some PbI<sub>2</sub> impurity (ICSD  
238 #52370) was also observed in the MA/PbI<sub>2</sub> and FA/PbI<sub>2</sub>  
239 systems due to the decomposition of the perovskite phases  
240 between synthesis and characterization.<sup>74,75</sup> Our ability to  
241 quickly explore possible reaction conditions to yield both  
242 MAPbI<sub>3</sub> and FAPbI<sub>3</sub> demonstrates the utility of RAPID for the  
243 formation of metal halide perovskites. Additional pXRD  
244 patterns indicate that orthorhombic EtAPbI<sub>3</sub><sup>76,77</sup> (Figure 3b),  
245 orthorhombic  $(\text{nBuA})_2\text{PbI}_4$ <sup>78,79</sup> (Figure 3c), and 13 other  
246 metal halide perovskites (Figures S7–S19) were crystallized  
247 using ITC methods. Powder XRD patterns from the Acet/PbI<sub>2</sub>  
248 system did not match simulated XRD patterns (Figure S20)  
249 for a calculated structure of AcetPbI<sub>3</sub>,<sup>80</sup> and no experimental  
250 structures have been reported for both Acet/PbI<sub>2</sub> and CHMA/  
251 PbI<sub>2</sub> systems (Figure 3e,f). This suggests that our high  
252 throughput experiments revealed the presence of two  
253 previously unknown compounds, which we confirmed below.  
254 To the best of our knowledge, ITC crystallization of the other  
255 17 compounds shown in Figures 3 and S7–S19 (excluding  
256 MAPbI<sub>3</sub> and FAPbI<sub>3</sub>) have not been previously reported,  
257 which demonstrates the utility of RAPID for discovering new  
258 synthetic routes. For the remaining 26 systems (i.e., those not  
259 shown in Figures 3 or S7–S19), nine of them produced large  
260 Class 4 crystals of unknown structures (i.e., unreported  
261 perovskite-derived phases, lead iodide or ammonium iodides,  
262 colored black in Figure 1) and another four cations produced  
263 Class 3 small crystals that are either perovskite-derived phases  
264 or unknown phases (marked with \*\* and \* respectively in  
265 Figure 1). The remaining 13 chemical systems (colored red in  
266 Figure 1, without marks) only produced Class 1, Class 2, or  
267 lead iodide crystals. The pXRD patterns for all 45 chemical  
268 systems are available through the interactive data visualization  
269 interface.<sup>68</sup> These results suggest that additional screening,  
270 supplemented by high-throughput XRD, may be necessary for  
271 identifying perovskite-derived phases in those systems.

272 **Crystal Structure Determination.** The use of high-  
273 throughput experimentation in the RAPID approach described  
274 here enables the direct elucidation and optimization of crystal  
275 growth conditions. The optimized reaction conditions,  
276 determined using RAPID, were then validated with bench  
277 scale reactions for each system. The result was the formation of  
278 very large (>1 mm), high-quality single crystals (Figure 4)  
279 without the need for subsequent optimization. Crystals from  
280 the MA/PbI<sub>2</sub> and FA/PbI<sub>2</sub> systems were dodecahedral,  
281 consistent with prior literature reports for their ITC  
282 syntheses.<sup>30,73</sup> Crystals from the EtA/PbI<sub>2</sub> systems were  
283 irregularly shaped, while reactions in the nBuA/PbI<sub>2</sub> and  
284 CHMA/PbI<sub>2</sub> systems produced flake-like crystals similar to  
285 those reported for 2D perovskite structures.<sup>78</sup> Reactions in the  
286 Acet/PbI<sub>2</sub> system resulted in yellow needle-like crystals. All of  
287 these large crystals are suitable for single crystal X-ray  
288 diffraction studies. The ability to grow such large, high quality

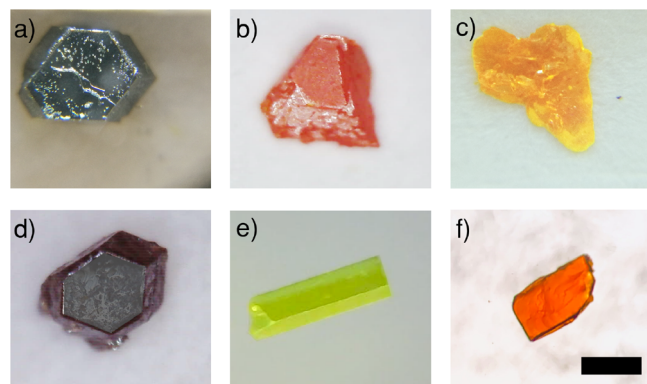


Figure 4. Optical micrographs of metal halide perovskite crystals produced by the MA/PbI<sub>2</sub> (a), EtA/PbI<sub>2</sub> (b), nBuA/PbI<sub>2</sub> (c), FA/PbI<sub>2</sub> (d), Acet/PbI<sub>2</sub> (e), and CHMA/PbI<sub>2</sub> systems (f). Scale bar: 1 mm.

crystals after a single set of high-throughput experiments will  
289 accelerate materials discovery.  
290

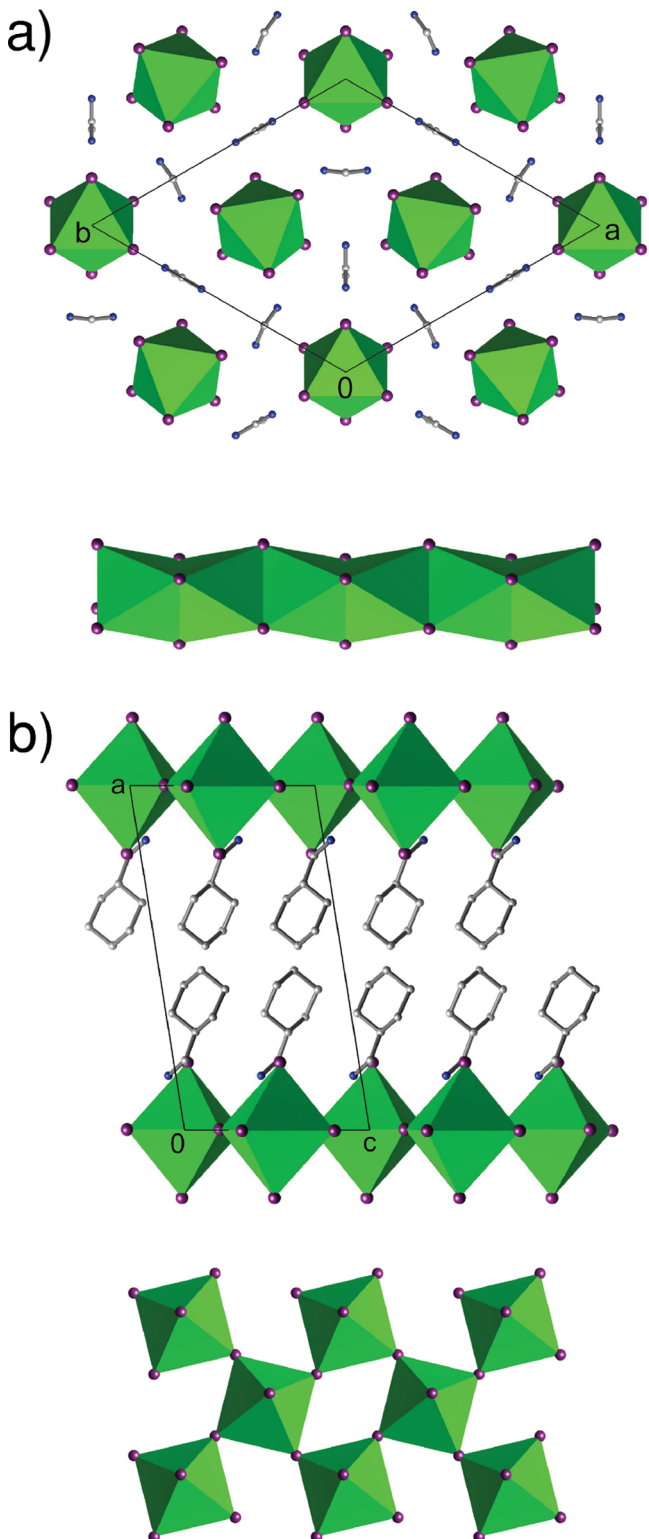
The yellow crystals shown in Figure 4e and the orange  
291 crystals in Figure 4f are based upon the unidentified phases in  
292 the Acet/PbI<sub>2</sub> and the CHMA/PbI<sub>2</sub> systems, respectively.  
293 Structural determination based on single-crystal X-ray  
294 diffraction confirmed two new phases: AcetPbI<sub>3</sub>, crystallizes  
295 in  $P31m$  while  $(\text{CHMA})_2\text{PbI}_4$  crystallizes in  $P2_1/c$ . Crystallographic  
296 details are provided in Table 1, while tables of bond  
297 lengths and angles are listed in the SI.  
298

Table 1. Crystallographic Data for AcetPbI<sub>3</sub> and  $(\text{CHMA})_2\text{PbI}_4$

compound	AcetPbI <sub>3</sub>	$(\text{CHMA})_2\text{PbI}_4$
formula	$\text{C}_2\text{H}_7\text{I}_3\text{N}_2\text{Pb}$	$\text{C}_{14}\text{H}_{32}\text{I}_4\text{N}_2\text{Pb}$
fw	646.98	943.24
space-group	$P31m$ (no. 157)	$P2_1/c$ (no. 14)
<i>a</i> (Å)	15.2648(6)	16.5155(8)
<i>b</i> (Å)	15.2648(6)	8.6521(5)
<i>c</i> (Å)	8.1332(3)	8.7642(4)
$\alpha$ (deg)	90	90
$\beta$ (deg)	90	99.0461(19)
$\gamma$ (deg)	120	90
<i>V</i> (Å <sup>3</sup> )	1641.25(14)	1236.77(11)
<i>Z</i>	6	2
$\rho_{\text{calc}}$ (g cm <sup>-3</sup> )	3.928	2.533
$\lambda$ (Å)	0.71073	0.71073
<i>T</i> (K)	100(2)	100(2)
$\mu$ (mm <sup>-1</sup> )	23.820	11.811
$R_1^a$	0.0365	0.0350
$wR_2^b$	0.0658	0.0935

<sup>a</sup> $R_1 = \|F_o\| - \|F_c\|/\|F_o\|$ . <sup>b</sup> $wR_2 = [w(F_o^2 - F_c^2)^2/w(F_o^2)]^{1/2}$

The structure of AcetPbI<sub>3</sub>, shown in Figure 5a, consists of one-dimensional  $[\text{PbI}_{6/2}]^-$  chains separated by  $[\text{AcetH}]^+$  cations. The  $[\text{PbI}_{6/2}]^-$  chains are constructed from face shared octahedra. The asymmetric unit contains four distinct lead sites and four distinct iodine sites. This results in two unique  $[\text{PbI}_{6/2}]^-$  chains, one of which contains Pb1, Pb2, I1 and I2, while the other contains Pb3, Pb4, I3, and I4. The Pb–I bonds range between 3.189(3) and 2.235(2) Å. The  $[\text{PbI}_{6/2}]^-$  chains are aligned along the *c*-axis. An extensive hydrogen-bonding network exists between the  $[\text{AcetH}]^+$  cations and  $[\text{PbI}_{6/2}]^-$



**Figure 5.** Three-dimensional packing and  $\text{[PbI}_{6/2}\text{]}^{-}$  chain structure in AcetPbI<sub>3</sub> (a) and the three-dimensional packing and  $\text{[PbI}_{2/\text{I}4/\text{2}}\text{]}^{2-}$  layer structure in (CHMA)<sub>2</sub>PbI<sub>4</sub> (b). Green polyhedra represent  $\text{[PbI}_6\text{]}$  octahedra, while purple, white, and blue atoms correspond to iodine, carbon, and nitrogen, respectively. Hydrogen atoms have been removed for clarity.

309 chains. The structure of AcetPbI<sub>3</sub> is similar to the recently  
 310 reported structure of pyrrolidinium lead iodide, which has a  
 311 narrow optical bandgap and decent water resistance.<sup>81</sup>

The structure of (CHMA)<sub>2</sub>PbI<sub>4</sub>, shown in Figure 5b,  
 312 contains two-dimensional  $\text{[PbI}_{2/\text{I}4/\text{2}}\text{]}^{2-}$  layers and  
 313 [CHMAH]<sup>+</sup> cations. The  $\text{[PbI}_{2/\text{I}4/\text{2}}\text{]}^{2-}$  layers are constructed  
 314 from corner shared octahedra. These layers are similar to those  
 315 found in Ruddlesden–Popper phase perovskites.<sup>78</sup> The  
 316 asymmetric unit contains a single lead site and two distinct  
 317 iodine sites. The Pb–I<sub>terminal</sub> bonds have distances of 3.2129(S)  
 318 Å, while the Pb–I<sub>bridging</sub> distances range between 3.1680(4) and  
 319 3.1729(4) Å. The  $\text{[PbI}_{2/\text{I}4/\text{2}}\text{]}^{2-}$  layers lie in the ab plane and  
 320 are separated by the organic cations. An extensive hydrogen-  
 321 bonding network exists between the [CHMAH]<sup>+</sup> cations and  
 322  $\text{[PbI}_{2/\text{I}4/\text{2}}\text{]}^{2-}$  layers. The ammonium sites on the [CHMAH]<sup>+</sup>  
 323 cations reside in the recesses within the  $\text{[PbI}_{2/\text{I}4/\text{2}}\text{]}^{2-}$  layers.  
 324 Details on the data collection, processing, and refinement of  
 325 single crystal X-ray diffraction data for AcetPbI<sub>3</sub> and  
 326 (CHMA)<sub>2</sub>PbI<sub>4</sub> can be found in the SI.  
 327

As expected for 1D hybrid perovskite structures, whose  
 328 electronic bands are less disperse than 3D perovskites,<sup>82</sup> the  
 329 electrical conductivity of AcetPbI<sub>3</sub> single crystals is low, falling  
 330 below the sensitivity limit of our measurement apparatus ( $2.8 \times 10^{-11}$  S/cm, see SI: Conductivity Measurement and Figure S24). UV–visible absorption spectra and the Tauc analyses  
 331 suggest that AcetPbI<sub>3</sub> and (CHMA)<sub>2</sub>PbI<sub>4</sub> have indirect  
 334 bandgaps of 2.11 and 2.22 eV, respectively (Figures S21 and  
 335 S22). While (CHMA)<sub>2</sub>PbI<sub>4</sub> exhibits a green emission peak at  
 336 536 nm (40 nm full width at half-maximum, fwhm), AcetPbI<sub>3</sub>  
 337 shows violet PL with an emission peak at 409 nm (54 nm  
 338 fwhm) (Figure S23). The color-pure and short-wavelength PL  
 339 makes AcetPbI<sub>3</sub> a potential candidate for violet and blue light-  
 340 emitting diodes. Violet or blue PL is rarely reported for 1D-  
 341 perovskite derivatives, which often show broader PL spectra at  
 342 longer wavelengths due to the formation of self-trapped  
 343 excitons.<sup>81,83–85</sup> Preliminary stability tests suggest that both  
 344 AcetPbI<sub>3</sub> and (CHMA)<sub>2</sub>PbI<sub>4</sub> are stable against humidity and  
 345 oxygen over periods longer than 7 months; as shown in Figure  
 346 S25, pXRD patterns of the two crystals exhibit no phase  
 347 changes after storage in air at room temperature under 23–  
 348 33% humidity. The identification and preliminary character-  
 349 ization of AcetPbI<sub>3</sub> and (CHMA)<sub>2</sub>PbI<sub>4</sub> demonstrate the utility  
 350 of RAPID to discover novel compounds with unexpected  
 351 properties and environmental stability. More extensive  
 352 investigations into the physical properties of the crystalline  
 353 materials isolated in this work will be described elsewhere.  
 354

**Quantifying Experimental Space and the Likelihood** of Single Crystal Formation. The comprehensive sampling of the experimental space, facilitated by RAPID, enables the rigorous statistical analysis of reaction outcomes. To quantify the number of possible experiments for a given set of stock solutions, we calculated the volume  $V_{\text{total}}$  inside the convex hull ( $C_{\text{total}}$ ) of the trials in the 19 crystallization screens which successfully result in the formation of large single crystals (Figures 2, S5, and S6). Here,  $C_{\text{total}}$  is the smallest convex polyhedral envelope containing all of the data points in multidimensional parameter space.<sup>86</sup> Differences in the reactant solubilities between organoammonium iodides result in convex hulls of different volumes. As shown in Figure 6b, the Piper/PbI<sub>2</sub> system exhibits the largest possible experimental space (as measured by  $C_{\text{total}}$ ) followed by nHex/PbI<sub>2</sub>, Morph/PbI<sub>2</sub>, and Acet/PbI<sub>2</sub> in descending order. The nDoda/PbI<sub>2</sub> system exhibits the smallest  $V_{\text{total}}$  because of the poor solubility of n-dodecylammonium iodide and lead iodide/n- dodecylammonium iodide mixtures in GBL.

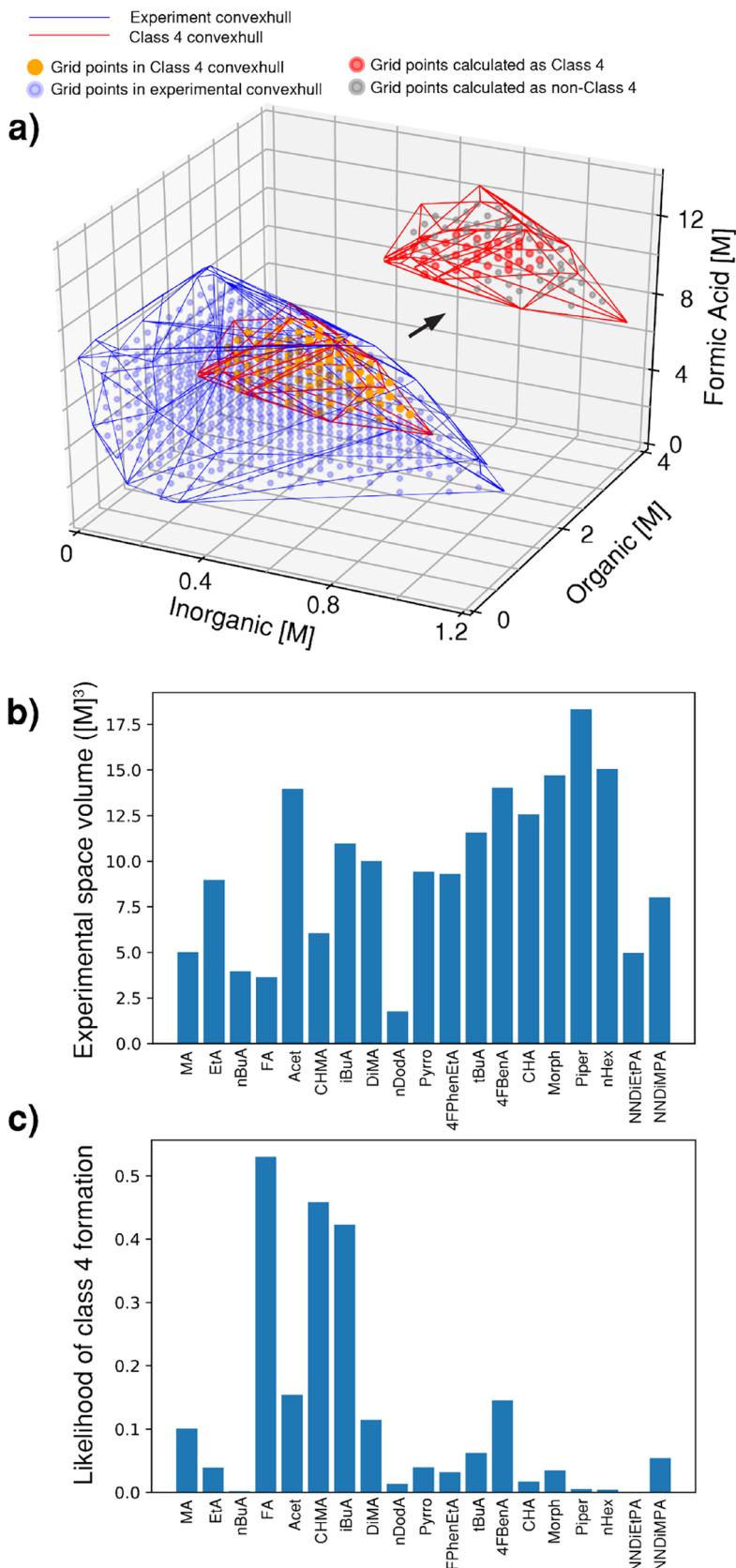


**Figure 6.** (a) Convex hulls, and the grid points contained within them, for the explored experimental space (blue lines/circles) and Class 4 outcomes (orange lines/circles), for the EtA/PbI<sub>2</sub> system at 95 °C. Inset: grid points within the Class 4 convex hull, with colors indicating Class 4 (red circles) and non-Class 4 (gray circles) outcomes as determined by the k-NN algorithm. (b) Convex hull volume of explored chemical space for all 19 perovskite syntheses. (c) Likelihood of large single crystal formation,  $P_4$ , for the 19 chemical systems studied.

To quantify the volume of the regions in which single crystals can be grown for each system, the convex hulls containing all Class 4 outcomes were calculated ( $C_4$ , outlined in red in Figure 6a).  $C_4$  includes some reactions that failed to generate single crystals (Classes 1–3, shaded in gray in Figure 6a), because the boundary between Class 4 and non-Class 4 is irregular. Therefore, the volume of  $C_4$  will not accurately measure reaction success. Alternatively, the naive approach of computing the ratio of number of successful reactions to the total number of observed reactions does not correctly describe the crystal formation probability because the distribution of reaction points is not homogeneous. A better estimate is obtained by interpolating the experimental data onto a uniform grid of points in the experimental space.  $C_{\text{total}}$  contains  $N_{\text{total}}$  of these grid points while  $C_4$  contains  $N_4$  points. Each grid point is assigned a crystal score using the 5 nearest experimental data points, following the  $k$ -nearest-neighbor ( $k$ -NN) algorithm with  $k = 5$  (see SI for additional details on algorithm). This is a computationally tractable approximation to the generalized higher-order Voronoi tessellation.<sup>87</sup> The subset of  $N_{(4)}$  grid points assigned to Class 4 scores using the  $k$ -NN method better accounts for the irregular (i.e., concave) envelopes. A graphical example is shown as an inset in Figure 6a for the EtA/PbI<sub>2</sub> system, with red circles denoting the  $N_{(4)}$  points assigned to Class 4 with other crystal scores ( $N_4 - N_{(4)}$ ) indicated by gray circles. The corresponding plots for the other perovskite syntheses are shown in the SI (Figures S26–S43).

The likelihood of Class 4 formation (defined as  $P_4 = N_{(4)} / N_{\text{total}}$ ) for the 19 systems in which metal halide perovskites were produced is shown in Figure 6c and Table S7. The FA/PbI<sub>2</sub>, CHMA/PbI<sub>2</sub>, and iBuA/PbI<sub>2</sub> systems show the highest likelihood of Class 4 crystal formation ( $P_4 = 0.53$ , 0.46, and 0.42 respectively) within the explored experimental space, followed by Acet/PbI<sub>2</sub> (0.15), 4FBenA/PbI<sub>2</sub> (0.15), DiMA/PbI<sub>2</sub> (0.11), and MA/PbI<sub>2</sub> (0.10). The other 12 systems show significantly lower  $P_4$  values (<0.1) which indicate that for these systems, the formation of large perovskite crystals is thermodynamically less favorable over the vast majority of experimental space. In the perovskite literature, the Goldschmidt tolerance factor (calculated from the effective ionic radius of A-cation, B-cation and X-anion in the perovskite structure: ABX<sub>3</sub>) is used to measure the stability and synthesizability of three-dimensional perovskite materials.<sup>1,88</sup> However, the 19 perovskite materials synthesized in this work are not necessarily three-dimensional. So the  $P_4$  value is not merely determined by the effective ionic radius but by a variety of factors. Single crystal formations were rarely observed for (nBuA)<sub>2</sub>PbI<sub>4</sub> and (NNDiEtPA)<sub>4</sub>Pb<sub>5</sub>I<sub>18</sub> syntheses, consistent with their low  $P_4$  of 0.002 and 0.0001. The ability to quickly visualize the state space in each system and to quantify the crystal growth probabilities is a direct result of the high-throughput, parallelized experimental data collection enabled by the RAPID approach.

**Machine Learning.** Synthetic chemistry data sets often exclude failed results (“dark reactions”)<sup>60</sup> and suffer from anthropogenic bias in experiment choices, limiting machine learning (ML) models trained on such data.<sup>89</sup> In contrast, RAPID’s combination of high-throughput experimentation, randomized reaction parameters and complete data capture is ideal for training and evaluating machine learning models. As a demonstration, we exported ESCALATE’s default set of 75 reaction conditions (e.g., concentrations, temperature, stir rate) and organic property descriptors (e.g., molecular weight,

atoms number, functional groups) and constructed a variety of machine learning models using the Scikit-Learn Python library (see SI and Methods for additional details). Binary classifier models were constructed to distinguish between experiments resulting in high quality single crystals (Class 4) and non-Class 4 outcomes. These models were applied to a base data set composed of the 4074 reactions in the 19 systems in which large crystals of metal halide perovskites were produced. Unless noted otherwise, each model was trained by randomly dividing the base data set into training and test sets (comprised of 80 and 20% of the data, respectively), with 5-fold cross-validation. The three models with the highest accuracy were as follows: Pearson VII Universal Function Kernel-based Support Vector Machine (PUFK-SVM),  $k$ -NN (where  $k = 1$ ) and Radial Basis Function Kernel-based Support Vector Machine (RBFK-SVM) with respective accuracies of 0.869, 0.845, and 0.841 (complete results, including metrics such as recall and precision, are listed in Table S8). Our prediction quality on these 19 systems exceeds the 13% accuracy demonstrated for a comparable task on 3-picolylammonium lead bromide in previous work.<sup>52</sup> The good performance of the 1-NN approach is indicative of an interpolation (rather than extrapolation) problem,<sup>90</sup> which in turn is indicative of the high quality of the full, quasi-random-sampled data set. Learning curves for the six representative perovskites previously highlighted in Figures 2–4 using the accuracy, precision, recall, and F1 scores are shown in Figures S44–S49. The learning curves of the other 13 successful systems can be viewed in the interactive data visualization and analysis interface.<sup>68</sup> Training data and Python implementations of all of the models are available both in the interactive data visualization browser<sup>68</sup> and on the supporting GitHub repository.<sup>69</sup>

The ML models described above can be used to reduce the number of experiments needed to accurately predict successful crystallization conditions. As a test, the data were separated by A-cation identity, with the PUFK-SVM model performance being considered as a function of the number of training examples for each A-cation type. As expected, model predictions become more accurate with an increasing number of training experiments (Figure 7a); the model for the Eta/PbI<sub>2</sub> system achieves prediction accuracy as high as 85% with only ~100 experiments. However, the flatness of the curves beyond 100 experiments indicates that a richer set of features (rather than more data) is needed to further improve the prediction quality. For (nBuA)<sub>2</sub>PbI<sub>4</sub>, the prediction accuracy decreases with an increasing number of training experiments, but this trend is an artifact of the low probability of Class 4 formation ( $P_4 = 0.002$ , Figure 6c). The early training rounds have no Class 4 outcomes, so the models are trained to predict only non-Class 4 outcomes, i.e., that all test samples will fail. The accuracy (formula given in the Software and Computation section in the SI) will be high even though the model fails to predict any of the positive outcomes. It is well-known that a heavily imbalanced distribution of class populations can result in accuracy values that do not capture the overall performance of the model, whereas the low precision and recall values for (nBuA)<sub>2</sub>PbI<sub>4</sub> (Figure S46) do. As the number of training samples increases, and the model starts to predict successes, the accuracy when modeling the imbalanced test set is reduced.

As it might be useful to be able to predict fine powder and small crystallite growth conditions, we trained binary classification models for Class 1, Class 2, and Class 3

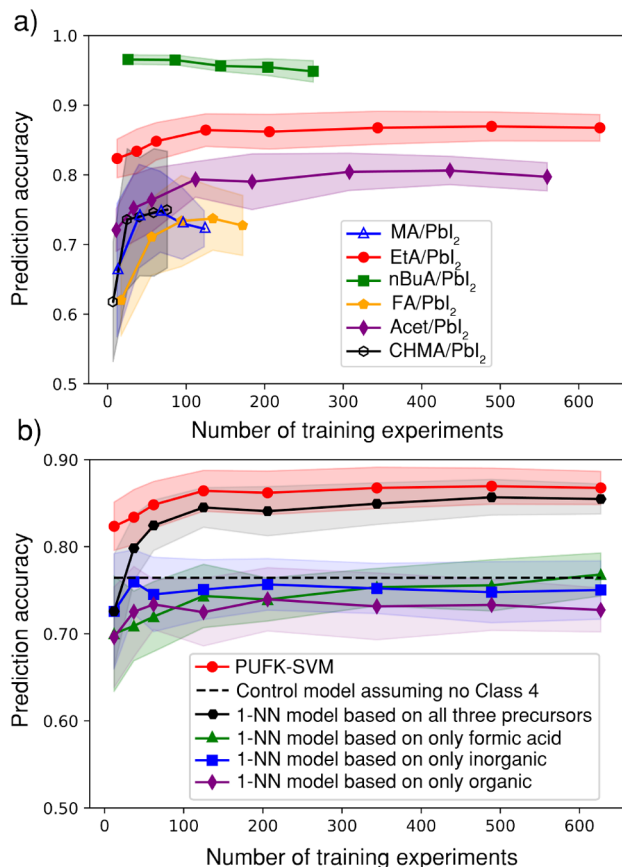


**Figure 7.** Learning curves for predicting perovskite crystal formation at 95 °C. (a) Prediction accuracy vs number of training experiments for PUFK-SVM models of the MA/PbI<sub>2</sub>, EtA/PbI<sub>2</sub>, nBuA/PbI<sub>2</sub>, FA/PbI<sub>2</sub>, Acet/PbI<sub>2</sub>, and CHMA/PbI<sub>2</sub> system crystallization. Solid lines show mean accuracy distinguishing between Class 4 and non-Class 4 outcomes; shaded bands indicate the standard deviation from 5-fold cross validation results for each system. (b) Accuracy predicting EtA/PbI<sub>2</sub> Class 4 crystal formation for six different models: PUFK-SVM; a control model assuming no Class 4 crystals (dashed line); 1-NN models ( $k = 1$ ) based on the concentrations of all three precursors (organic, inorganic, formic acid); and 1-NN models based on only one precursor.

500 outcomes, individually, for the case of EtAPbI<sub>3</sub> case (e.g., Class 501 X = positive, non-Class X = negative, for X = 1, 2, 3). These 502 results are shown in Figure S51. We found that our machine 503 learning model (SVM with Pearson VII kernel) has the best 504 performance predicting Class 1 (clear solutions) while having 505 the lowest prediction metrics for Class 3. Predicting Class 2 506 outcomes is similar in performance to predicting Class 4 507 results. We hypothesize that the ML performance for different 508 classes could be largely influenced by their distribution in 509 experimental space (see Figure 2). Class 1 is easy to predict by 510 the model as its reactions are distributed almost exclusively in a 511 regularly shaped convex hull in the experimental space. The 512 irregular distribution of Class 3 outcomes in the narrow space 513 between Class 4 and Class 2 makes it the most difficult to 514 predict.

515 ML models can assist in determining which experimental 516 parameters contribute the most to the accuracy of the 517 prediction, providing physical insight. As an illustrative 518 example, we considered the EtA/PbI<sub>2</sub> system using only the 519 concentrations of the organic, inorganic, and formic acid

species. As depicted in Figure 7b, a PUFK-SVM model (red) 520 trained exclusively on EtA/PbI<sub>2</sub> system data resulted in the 521 highest performance, plateauing at 87% accuracy. For 522 comparison, the control model (dashed line) that predicts 523 every reaction to fail has 76% accuracy. Therefore, the PUFK- 524 SVM predictions are significantly better than random chance. 525 A 1-NN model (i.e., a  $k$ -NN with  $k = 1$ ) in this three- 526 dimensional feature space is 1–2% lower in absolute accuracy 527 than the PUFK-SVM after 100 training experiments. This 1- 528 NN algorithm is equivalent to using the most similar past 529 reaction outcome as a prediction, and the high sample density 530 of our data set facilitates this approach. Importantly, we find 531 that the combination of the three reactant concentrations is 532 meaningful. We demonstrated this by generating 1-NN models 533 that only consider the concentration of a single reagent (green, 534 blue, and purple lines in Figure 7b). These single variable 535 models are less accurate than the control model, indicating that 536 they have no predictive value. Taken together, these data 537 support the reasonable conclusion that crystal quality is not 538 determined by the concentration of a single chemical species, 539 but instead depends on the concentrations of all species. 540

ML models can help generalize understanding across both 541 reactions and reagent choices. As a demonstration, we used the 542 PUFK-SVM model to predict reaction outcomes for each of 543 the six representative perovskite systems studied given the 544 following two training/testing strategies. The first strategy 545 trained models using data only from the perovskite of interest. 546 This baseline strategy corresponds to beginning the study of 547 each organic cation with a tabula rasa. The second strategy 548 trained ML models for a given cation of interest using data 549 from the other N-1 organic cations as well. In principle, 550 training data from other cations should improve prediction 551 quality if the model can extract generalizable trends from the 552 available chemical descriptors. However, the accuracies for 553 both strategies (shown in Figure S50) are statistically 554 indistinguishable for all cations tested, indicating that, despite 555 the ability to generalize across reaction conditions (vide supra) 556 for a single cation, the models do not generalize across 557 different cations. This could arise from the limitations of the 558 current chemical descriptors or from the type of reaction 559 outcomes we choose to model. Our current research efforts are 560 aimed at addressing this issue, e.g., by incorporating new 561 molecular embeddings and reaction representations pertaining 562 to crystal formation. 563

## CONCLUSIONS

We have developed an automated, high-throughput robotic 565 synthesis platform (Robot-Accelerated Perovskite Investigation 566 and Discovery, or RAPID) for metal halide perovskite single 567 crystal discovery. A total of 8172 reactions were performed 568 using our RAPID workflow, spanning the large experimental 569 space of inverse temperature crystallization in only ~400 h of 570 unattended operation. For comparison, the same number of 571 reactions performed manually, at 10 reactions per day, would 572 require over 800 days, or over 6000 h of human labor. We 573 identified conditions that produce perovskite single crystals for 574 19 out of 45 target perovskite compositions, adding 17 new 575 materials to the library of metal halide perovskites accessible 576 via ITC (a 400% increase). Among these compounds are two 577 novel perovskite species, AcetPbI<sub>3</sub> and (CHMA)<sub>2</sub>PbI<sub>4</sub>, for 578 which we reported the crystal structures and performed 579 preliminary characterization. Our RAPID data set allowed us 580 to quantify the probability of randomly finding a condition that 581

582 produces single crystals. We also demonstrated the use of this  
583 data set to train machine learning models to improve common  
584 materials discovery tasks. Less than 100 experiments are  
585 typically required to build an informative model for a new  
586 organic cation species, but the current data set and features  
587 preclude generalization across organic cations. This initial  
588 study emphasizes the need to expand the chemical library and  
589 physicochemical descriptors<sup>91</sup> to further improve the ability of  
590 ML models to predict the crystallization conditions of new  
591 organic–inorganic metal halide perovskites. Nonetheless,  
592 RAPID is a powerful tool for accelerating perovskite discovery  
593 and can be readily extended to a broad range of synthetic  
594 routes and materials.<sup>91,92</sup>

## 595 ■ EXPERIMENTAL SECTION

596 **Materials.** All reagents were purchased from commercial sources  
597 and used without further purification. Lead iodide, formic acid,  
598 dimethyl sulfoxide (DMSO), and dimethylformamide (DMF) were  
599 purchased from Sigma-Aldrich with 99%, ≥ 95%, ≥ 99.5%, and 99.8%  
600 purity, respectively.  $\gamma$ -Butyrolactone (GBL) (≥98%) was purchased  
601 from Spectrum Chemical. All 45 ammonium iodides used in this work  
602 were purchased from GreatCell Solar with purity ≥98%.

603 **Stock Solutions and Solubility Measurements.** Before each  
604 robotic synthesis, stock solutions (ammonium iodide stocks and  
605 stocks containing mixtures of PbI<sub>2</sub>/ammonium iodide) were prepared  
606 manually based on the solubility of these compounds. To determine  
607 the maximum solubility of lead iodide in a given solvent (GBL,  
608 DMSO, or DMF) and for a given ammonium iodide concentration,  
609 lead iodide was mixed with different amounts of a selected  
610 ammonium iodide and then the solvent was added gradually into  
611 the mixtures until the solids were completely dissolved. During the  
612 dissolution process, suspensions were stirred and heated in an oil bath  
613 at 450 rpm and 75 °C. The resulting solutions were allowed to cool to  
614 room temperature to confirm their stability. The solubilities of pure  
615 ammonium iodides were measured using the same procedure.  
616 Solubility data for lead iodide and individual ammonium iodides are  
617 shown in Table S2. All stock solutions were used within 8 h of their  
618 preparation,

619 **Robotic Synthesis Workflow.** High-throughput synthesis of  
620 metal halide perovskite single crystals was performed with a Hamilton  
621 Microlab NIMBUS4 liquid handling robot equipped with four  
622 independent micropipettors. Robotic protocols, programmed in  
623 Hamilton Method Editor software, imported experiment-specific  
624 reaction parameters, such as reagent volumes, reaction times, and  
625 shaking speeds, from Microsoft Excel.xls spreadsheets generated by  
626 the ESCALATE<sup>64</sup> software pipeline. In addition to specifying  
627 experimental parameters, ESCALATE was used to capture exper-  
628 imental results and observations following characterization of the  
629 products.

630 Reaction components (i.e., the stock solutions, pure solvent, and  
631 formic acid) were placed in designated locations on NIMBUS  
632 operation deck, as shown in Figure S4. Glass scintillation vials (8 × 43  
633 mm<sup>2</sup> diameter × height), which served as reaction vessels, were  
634 loaded into a 96-well aluminum microplate (Symyx Technologies),  
635 which was placed on a Hamilton Heater Shaker II (HHS2) module  
636 on the Nimbus deck. Robot protocols were then initiated, beginning  
637 with preheating the 96 empty vials in the HHS2 to 105 °C set  
638 temperature. After the HHS2 temperature reached 80 °C, the liquid  
639 handling robot dispensed into each reaction vial specified amounts of  
640 the pure solvent, PbI<sub>2</sub>/ammonium iodide stock solution, ammonium  
641 iodide stock solution, and formic acid. The microplate was then  
642 vortexed at 750 rpm for 15 min, followed by dispensing of a second  
643 cycle of formic acid. After another 20 min of vortexing at 750 rpm, the  
644 resulting solutions were held at an actual solution temperature of 95  
645 °C (105 °C set temperature) without shaking for 2.5 h to allow for  
646 crystal growth. During crystallization, the Nimbus robot was left  
647 undisturbed, and air convection was minimized by closing the sash of

the fume hood. Additional details are given in the “[Robotic Workflow](#)” section and [Step-by-Step Robotic Procedure](#) in the SI.

648  
649 **Crystal Scoring.** To score reaction outcomes, reaction vials were  
650 inspected at different angles by eye. Reaction outcomes were scored  
651 into four classes. Class 1: no solid observed in the solutions. Class 2:  
652 fine powder observed with no visible crystal facets; under  
653 illumination, reflection is diffuse rather than specular. Class 3: small  
654 crystallites with approximate size 0.1 mm or smaller; distinct from  
655 Class 2 in exhibiting specular reflection at certain angles, indicating  
656 the presence of crystal facets. Class 4: large crystals (>0.1 mm) with  
657 straight edges and large area of specular reflection from crystal facets.  
658 When multiple crystal types were observed in the same vial, we used  
659 the highest score for each reaction.

660  
661 **Characterization.** Powder X-ray diffraction measurements were  
662 performed on a Bruker AXS D8 Discover GADDS X-ray  
663 Diffractometer equipped with a Vantec-500 area detector operated  
664 at 35 kV/40 mA using Co K $\alpha$  radiation (1.79 Å wavelength). Diffuse  
665 reflectance UV–visible absorption spectra of powders ground from  
666 large perovskite crystals were measured with an Agilent Cary-5000  
667 UV–vis–NIR spectrophotometer. Photoluminescence spectra (PL)  
668 of powders ground from large perovskite crystals were measured using  
669 a Horiba Jobin Yvon Fluorolog-3 spectrofluorometer. PL spectra were  
670 collected from 365 to 650 nm with 1 nm wavelength steps and 0.01 s  
671 integration time per step. Conductivity measurements were  
672 performed on needle-shaped AcetPbI<sub>3</sub> single crystals (with lengths  
673 of 0.3–0.6 mm) using a customized probe station. The needle crystals  
674 were placed on double-sided tape on clean glass slides and carbon  
675 paste was applied at opposite ends of the needle crystals as electrodes.  
676 In this configuration, the cross-sectional area of electron transport is  
677 approximately the cross-sectional area of the needle crystals, which is  
678 in the range of 0.3–0.4 mm<sup>2</sup>. Platinum probes were placed to form  
679 contacts with carbon electrodes, and a Keithley 2400 source meter  
680 was used to measure  $I$ – $V$  curves.

681  
682 **Software and Machine Learning.** Scripts for data analysis and  
683 visualization were written in Python 3.6 in Jupyter notebooks using  
684 the following libraries: Numpy 1.14.6, Pandas 0.22.0, Scipy 1.0.1, 685  
686 Matplotlib 3.1.0 and Scikit-learn 0.19.2. We used the Quickhull  
687 algorithm implemented in Scipy to calculate the convex hull. For  
688 machine learning, a total of 75 features were selected to describe each  
689 perovskite single crystal synthesis reaction. Those features include  
690 eight reaction conditions and 67 computed property descriptors of  
691 organoammonium. Detailed explanations for the features used in this  
692 work are listed in Section 3 of the SI ([Explanation of Features/](#)  
693 Descriptors for Machine Learning Modeling). Experimental results  
694 were analyzed as a binary classification problem: Class 4 outcomes  
695 were considered as positive results while non-Class 4 outcomes were  
696 considered as negative results. A 5-fold cross-validation procedure was  
697 used to prepare training/testing data sets for machine learning  
698 modeling. For 5-fold cross-validation, there were 5 different train/test  
699 splits on the data set: in each split, 80% of the data was randomly  
700 drawn to train the machine learning model, while the remaining 20%  
701 of the data was reserved for testing. Model hyper-parameters were  
702 optimized using a grid search method with 5-fold cross-validation for  
703 highest prediction accuracy.

## 704 ■ ASSOCIATED CONTENT

### 705 **SI Supporting Information**

706 The Supporting Information is available free of charge at  
707 <https://pubs.acs.org/doi/10.1021/acs.chemmater.0c01153>.

708  
709 Detailed materials and methods; instructions for  
710 interactively visualizing and downloading data sets for  
711 all 45 chemical systems studied in this work; photo-  
712 graphs of representative crystals; additional crystal  
713 quality plots and XRD patterns for 13 perovskite  
714 systems not shown in the main text; solubility data for  
715 all perovskite systems in this work; single crystal  
716 structure refinement, absorption spectra, PL spectra,  
717 electrical conductivity, and stability tests for AcetPbI<sub>3</sub>

and  $(\text{CHMA})_2\text{PbI}_4$ ; additional convex hull plots and data; additional tables and training curves summarizing prediction metrics for machine learning models; and features and descriptors used for training machine learning models ([PDF](#))  
Crystallographic data of  $\text{AcetPbI}_3$  ([CIF](#))  
Crystallographic data of  $(\text{CHMA})_2\text{PbI}_4$  ([CIF](#))

## AUTHOR INFORMATION

### Corresponding Authors

**Joshua Schrier** — Department of Chemistry, Haverford College, Haverford, Pennsylvania 19041, United States; Department of Chemistry, Fordham University, The Bronx, New York 10458, United States;  [orcid.org/0000-0002-2071-1657](#); Email: [jschrier@fordham.edu](mailto:jschrier@fordham.edu)  
**Alexander J. Norquist** — Department of Chemistry, Haverford College, Haverford, Pennsylvania 19041, United States; Email: [anorquis@haverford.edu](mailto:anorquis@haverford.edu)  
**Emory M. Chan** — Molecular Foundry, Lawrence Berkeley National Laboratory, Berkeley, California 94720, United States;  [orcid.org/0000-0002-5655-0146](#); Email: [EMChan@lbl.gov](mailto:EMChan@lbl.gov)

### Authors

**Zhi Li** — Molecular Foundry, Lawrence Berkeley National Laboratory, Berkeley, California 94720, United States  
**Mansoor Ani Najeeb** — Department of Chemistry, Haverford College, Haverford, Pennsylvania 19041, United States  
**Liana Alves** — Department of Chemistry, Haverford College, Haverford, Pennsylvania 19041, United States; Molecular Foundry, Lawrence Berkeley National Laboratory, Berkeley, California 94720, United States  
**Alyssa Z. Sherman** — Department of Chemistry, Haverford College, Haverford, Pennsylvania 19041, United States  
**Venkateswaran Shekar** — Department of Computer Science, Haverford College, Haverford, Pennsylvania 19041, United States  
**Peter Cruz Parrilla** — Department of Chemistry, Haverford College, Haverford, Pennsylvania 19041, United States  
**Ian M. Pendleton** — Department of Chemistry, Haverford College, Haverford, Pennsylvania 19041, United States  
**Wesley Wang** — Molecular Foundry, Lawrence Berkeley National Laboratory, Berkeley, California 94720, United States; Department of Chemistry, University of California, Berkeley, Berkeley, California 94720, United States  
**Philip W. Nega** — Molecular Foundry, Lawrence Berkeley National Laboratory, Berkeley, California 94720, United States  
**Matthias Zeller** — Department of Chemistry, Purdue University, West Lafayette, Indiana 47907, United States;  [orcid.org/0000-0002-3305-852X](#)

Complete contact information is available at:

<https://pubs.acs.org/10.1021/acs.chemmater.0c01153>

### Notes

The authors declare no competing financial interest.

## ACKNOWLEDGMENTS

This study is based upon work supported by the Defense Advanced Research Projects Agency (DARPA) under Contract No. HR001118C0036. Any opinions, findings, and conclusions or recommendations expressed in this material are those of the authors and do not necessarily reflect the views of DARPA.

Work at the Molecular Foundry was supported by the Office of Science, Office of Basic Energy Sciences, of the U.S. Department of Energy under Contract No. DE-AC02-05CH11231. L.A. and J.S. were supported in part by the U.S. Department of Energy, Office of Science, Office of Workforce Development for Teachers and Scientists (WDTD) under the Visiting Faculty Program (VFP) and Berkeley Lab Undergraduate Faculty Fellowship (BLUFF). J.S. acknowledges the Henry Dreyfus Teacher-Scholar Award (TH-14-010). M.Z. acknowledges the National Science Foundation Major Research Instrumentation Program under Grant No. CHE 1625543, for funding for the single crystal X-ray diffractometer.

## REFERENCES

- (1) Saparov, B.; Mitzi, D. B. Organic–Inorganic Perovskites: Structural Versatility for Functional Materials Design. *Chem. Rev.* **2016**, *116*, 4558–4596.
- (2) Mitzi, D. B.; Feild, C. A.; Schlesinger, Z.; Laibowitz, R. B. Transport, Optical, and Magnetic Properties of the Conducting Halide Perovskite  $\text{CH}_3\text{NH}_3\text{SnI}_3$ . *J. Solid State Chem.* **1995**, *114*, 159–163.
- (3) Herz, L. M. Charge-Carrier Mobilities in Metal Halide Perovskites: Fundamental Mechanisms and Limits. *ACS Energy Lett.* **2017**, *2*, 1539–1548.
- (4) Xing, G.; Mathews, N.; Sun, S.; Lim, S. S.; Lam, Y. M.; Grätzel, M.; Mhaisalkar, S.; Sum, T. C. Long-Range Balanced Electron- and Hole-Transport Lengths in Organic-Inorganic  $\text{CH}_3\text{NH}_3\text{PbI}_3$ . *Science* **2013**, *342*, 344–347.
- (5) Zhao, Y.; Zhu, K. Organic–Inorganic Hybrid Lead Halide Perovskites for Optoelectronic and Electronic Applications. *Chem. Soc. Rev.* **2016**, *45*, 655–689.
- (6) Takahashi, Y.; Obara, R.; Nakagawa, K.; Nakano, M.; Tokita, J.; Inabe, T. Tunable Charge Transport in Soluble Organic–Inorganic Hybrid Semiconductors. *Chem. Mater.* **2007**, *19*, 6312–6316.
- (7) Veldhuis, S. A.; Boix, P. P.; Yantara, N.; Li, M.; Sum, T. C.; Mathews, N.; Mhaisalkar, S. G. Perovskite Materials for Light-Emitting Diodes and Lasers. *Adv. Mater.* **2016**, *28*, 6804–6834.
- (8) Wang, H.-C.; Bao, Z.; Tsai, H.-Y.; Tang, A.-C.; Liu, R.-S. Perovskite Quantum Dots and Their Application in Light-Emitting Diodes. *Small* **2018**, *14*, 1702433–1702455.
- (9) Deschler, F.; Price, M.; Pathak, S.; Klintberg, L. E.; Jarausch, D.; Higler, R.; Hüttner, S.; Leijtens, T.; Stranks, S. D.; Snaith, H. J.; et al. High Photoluminescence Efficiency and Optically Pumped Lasing in Solution-Processed Mixed Halide Perovskite Semiconductors. *J. Phys. Chem. Lett.* **2014**, *5*, 1421–1426.
- (10) Hu, X.; Zhang, X.; Liang, L.; Bao, J.; Li, S.; Yang, W.; Xie, Y. High-Performance Flexible Broadband Photodetector Based on Organolead Halide Perovskite. *Adv. Funct. Mater.* **2014**, *24*, 7373–7380.
- (11) Li, F.; Ma, C.; Wang, H.; Hu, W.; Yu, W.; Sheikh, A. D.; Wu, T. Ambipolar Solution-Processed Hybrid Perovskite Phototransistors. *Nat. Commun.* **2015**, *6*, 8238.
- (12) Lee, W.; Li, H.; Wong, A. B.; Zhang, D.; Lai, M.; Yu, Y.; Kong, Q.; Lin, E.; Urban, J. J.; Grossman, J. C.; et al. Ultralow Thermal Conductivity in All-Inorganic Halide Perovskites. *Proc. Natl. Acad. Sci. U. S. A.* **2017**, *114*, 8693–8697.
- (13) Pisoni, A.; Jaćimović, J.; Barišić, O. S.; Spina, M.; Gaál, R.; Forró, L.; Horváth, E. Ultra-Low Thermal Conductivity in Organic–Inorganic Hybrid Perovskite  $\text{CH}_3\text{NH}_3\text{PbI}_3$ . *J. Phys. Chem. Lett.* **2014**, *5*, 2488–2492.
- (14) Correa-Baena, J.-P.; Abate, A.; Saliba, M.; Tress, W.; Jacobsson, T. J.; Grätzel, M.; Hagfeldt, A. The Rapid Evolution of Highly Efficient Perovskite Solar Cells. *Energy Environ. Sci.* **2017**, *10*, 710–727.
- (15) Zhou, Y.; Game, O. S.; Pang, S.; Padture, N. P. Microstructures of Organometal Trihalide Perovskites for Solar Cells: Their Evolution of

- 839 from Solutions and Characterization. *J. Phys. Chem. Lett.* **2015**, *6*,  
840 4827–4839.
- 841 (16) Correa-Baena, J.-P.; Saliba, M.; Buonassisi, T.; Grätzel, M.;  
842 Abate, A.; Tress, W.; Hagfeldt, A. Promises and Challenges of  
843 Perovskite Solar Cells. *Science* **2017**, *358*, 739–744.
- 844 (17) Giustino, F.; Snaith, H. J. Toward Lead-Free Perovskite Solar  
845 Cells. *ACS Energy Lett.* **2016**, *1*, 1233–1240.
- 846 (18) Huang, J.; Yuan, Y.; Shao, Y.; Yan, Y. Understanding the  
847 Physical Properties of Hybrid Perovskites for Photovoltaic Applica-  
848 tions. *Nat. Rev. Mater.* **2017**, *2*, 17042.
- 849 (19) Wang, R.; Mujahid, M.; Duan, Y.; Wang, Z.-K.; Xue, J.; Yang, Y.  
850 A Review of Perovskites Solar Cell Stability. *Adv. Funct. Mater.* **2019**,  
851 *29*, 1808843–1808867.
- 852 (20) Best Research-Cell Efficiency Chart | Photovoltaic Research |  
853 NREL <https://www.nrel.gov/pv/cell-efficiency.html> (accessed Jun  
854 24, 2019).
- 855 (21) Leveillee, J.; Katan, C.; Even, J.; Ghosh, D.; Nie, W.; Mohite, A.  
856 D.; Tretiak, S.; Schleife, A.; Neukirch, A. J. Tuning Electronic  
857 Structure in Layered Hybrid Perovskites with Organic Spacer  
858 Substitution. *Nano Lett.* **2019**, *19*, 8732–8740.
- 859 (22) Yang, C.; Peng, Y.; Simon, T.; Cui, T. Control of PbI<sub>2</sub>  
860 Nucleation and Crystallization: Towards Efficient Perovskite Solar  
861 Cells Based on Vapor-Assisted Solution Process. *Mater. Res. Express*  
862 **2018**, *5*, 045507–045516.
- 863 (23) Yin, J.; Qu, H.; Cao, J.; Tai, H.; Li, J.; Zheng, N. Vapor-Assisted  
864 Crystallization Control toward High Performance Perovskite Photo-  
865 voltaics with over 18% Efficiency in the Ambient Atmosphere. *J.  
866 Mater. Chem. A* **2016**, *4*, 13203–13210.
- 867 (24) Deng, W.; Huang, L.; Xu, X.; Zhang, X.; Jin, X.; Lee, S.-T.; Jie,  
868 J. Ultrahigh-Responsivity Photodetectors from Perovskite Nanowire  
869 Arrays for Sequentially Tunable Spectral Measurement. *Nano Lett.*  
870 **2017**, *17*, 2482–2489.
- 871 (25) Shi, D.; Adinolfi, V.; Comin, R.; Yuan, M.; Alarousu, E.; Buin,  
872 A.; Chen, Y.; Hoogland, S.; Rothenberger, A.; Katsiev, K.; et al. Low  
873 Trap-State Density and Long Carrier Diffusion in Organolead  
874 Trihalide Perovskite Single Crystals. *Science* **2015**, *347*, 519–522.
- 875 (26) Dong, Q.; Fang, Y.; Shao, Y.; Mulligan, P.; Qiu, J.; Cao, L.;  
876 Huang, J. Electron-Hole Diffusion Lengths > 175 μm in Solution-  
877 Grown CH<sub>3</sub>NH<sub>3</sub>PbI<sub>3</sub> Single Crystals. *Science* **2015**, *347*, 967–970.
- 878 (27) Yue, H.-L.; Sung, H.-H.; Chen, F.-C. Seeded Space-Limited  
879 Crystallization of CH<sub>3</sub>NH<sub>3</sub>PbI<sub>3</sub> Single-Crystal Plates for Perovskite  
880 Solar Cells. *Adv. Electron. Mater.* **2018**, *4*, 1700655.
- 881 (28) Liao, W.-Q.; Zhang, Y.; Hu, C.-L.; Mao, J.-G.; Ye, H.-Y.; Li, P.-  
882 F.; Huang, S. D.; Xiong, R.-G. A Lead-Halide Perovskite Molecular  
883 Ferroelectric Semiconductor. *Nat. Commun.* **2015**, *6*, 7338–7344.
- 884 (29) Shi, C.; Ye, L.; Gong, Z.-X.; Ma, J.-J.; Wang, Q.-W.; Jiang, J.-Y.;  
885 Hua, M.-M.; Wang, C.-F.; Yu, H.; Zhang, Y.; et al. Two-Dimensional  
886 Organic-Inorganic Hybrid Rare-Earth Double Perovskite Ferro-  
887 electrics. *J. Am. Chem. Soc.* **2020**, *142*, 545–551.
- 888 (30) Saidaminov, M. I.; Abdelhady, A. L.; Murali, B.; Alarousu, E.;  
889 Burlakov, V. M.; Peng, W.; Dursun, I.; Wang, L.; He, Y.; Maculan, G.;  
890 et al. High-Quality Bulk Hybrid Perovskite Single Crystals within  
891 Minutes by Inverse Temperature Crystallization. *Nat. Commun.* **2015**,  
892 *6*, 7586–7592.
- 893 (31) Desai, S. Inverse Temperature Crystallization of Perovskite  
894 Material Methylammonium Lead Triiodide (CH<sub>3</sub>NH<sub>3</sub>PbI<sub>3</sub>) and Its  
895 Applications for Energy Storage. Master's thesis, Lamar University:  
896 Beaumont, TX, 2017.
- 897 (32) Han, C.; Wei, Z.; Wang, K.; Yu, H.; Deng, L.; Zhu, X.; Yang,  
898 H.; Sun, X.; Zhao, F.; Zhang, Q.; et al. Effect of Surface  
899 Recombination in High Performance White-Light CH<sub>3</sub>NH<sub>3</sub>PbI<sub>3</sub>  
900 Single Crystal Photodetectors. *Opt. Express* **2018**, *26*, 26307–26316.
- 901 (33) Wang, K.-H.; Li, L.-C.; Shellaiah, M.; Sun, K. W. Structural and  
902 Photophysical Properties of Methylammonium Lead Tribromide  
903 (MAPbBr<sub>3</sub>) Single Crystals. *Sci. Rep.* **2017**, *7*, 13643–13656.
- 904 (34) Kadro, J. M.; Nonomura, K.; Gachet, D.; Grätzel, M.; Hagfeldt,  
905 A. Facile Route to Freestanding CH<sub>3</sub>NH<sub>3</sub>PbI<sub>3</sub> Crystals Using Inverse  
906 Solubility. *Sci. Rep.* **2015**, *5*, 11654–11663.
- 907 (35) Najeeb, M. A.; Ahmad, Z.; Shakoor, R. A.; Alashraf, A.; Bhadra,  
908 J.; Al-Thani, N. J.; Al-Muhtaseb, S. A.; Mohamed, A. M. A. Growth of  
909 MAPbBr<sub>3</sub> Perovskite Crystals and Its Interfacial Properties with Al  
910 and Ag Contacts for Perovskite Solar Cells. *Opt. Mater.* **2017**, *73*, 50–  
911 55.
- 912 (36) Zhumekenov, A. A.; Saidaminov, M. I.; Haque, M. A.;  
913 Alarousu, E.; Samah, S. P.; Murali, B.; Dursun, I.; Miao, X.-H.;  
914 Abdelhady, A. L.; Wu, T.; et al. Formamidinium Lead Halide  
915 Perovskite Crystals with Unprecedented Long Carrier Dynamics and  
916 Diffusion Length. *ACS Energy Lett.* **2016**, *1*, 32–37.
- 917 (37) Chan, E. M.; Xu, C.; Mao, A. W.; Han, G.; Owen, J. S.; Cohen,  
918 B. E.; Milliron, D. J. Reproducible, High-Throughput Synthesis of  
919 Colloidal Nanocrystals for Optimization in Multidimensional  
920 Parameter Space. *Nano Lett.* **2010**, *10*, 1874–1885.
- 921 (38) Maryasin, B.; Marquetand, P.; Maulide, N. Machine Learning  
922 for Organic Synthesis: Are Robots Replacing Chemists? *Angew.  
923 Chem., Int. Ed.* **2018**, *57*, 6978–6980.
- 924 (39) Ahneman, D. T.; Estrada, J. G.; Lin, S.; Dreher, S. D.; Doyle, A.  
925 G. Predicting Reaction Performance in C–N Cross-Coupling Using  
926 Machine Learning. *Science* **2018**, *360*, 186–190.
- 927 (40) Lin, S.; Dikler, S.; Blincoe, W. D.; Ferguson, R. D.; Sheridan, R.  
928 P.; Peng, Z.; Conway, D. V.; Zawatzky, K.; Wang, H.; Cernak, T.;  
929 et al. Mapping the Dark Space of Chemical Reactions with Extended  
930 Nanomole Synthesis and MALDI-TOF MS. *Science* **2018**, *361*, 930  
eaar6236.
- 931 (41) Shevlin, M. Practical High-Throughput Experimentation for  
932 Chemists. *ACS Med. Chem. Lett.* **2017**, *8*, 601–607.
- 933 (42) Nikolaev, P.; Hooper, D.; Webber, F.; Rao, R.; Decker, K.;  
934 Krein, M.; Poleski, J.; Barto, R.; Maruyama, B. Autonomy in Materials  
935 Research: A Case Study in Carbon Nanotube Growth. *npj Comput.  
936 Mater.* **2016**, *2*, 16031.
- 937 (43) Duros, V.; Grizou, J.; Xuan, W.; Hosni, Z.; Long, D.-L.; Miras,  
938 H. N.; Cronin, L. Human versus Robots in the Discovery and  
939 Crystallization of Gigantic Polyoxometalates. *Angew. Chem., Int. Ed.*  
940 **2017**, *56*, 10815–10820.
- 941 (44) Ren, F.; Ward, L.; Williams, T.; Laws, K. J.; Wolverton, C.;  
942 Hattrick-Simpers, J.; Mehta, A. Accelerated Discovery of Metallic  
943 Glasses through Iteration of Machine Learning and High-Throughput  
944 Experiments. *Sci. Adv.* **2018**, *4*, eaal1566.
- 945 (45) Reinhardt, E.; Salaheldin, A. M.; Distaso, M.; Segets, D.;  
946 Peukert, W. Rapid Characterization and Parameter Space Exploration  
947 of Perovskites Using an Automated Routine. *ACS Comb. Sci.* **2020**, *22*,  
948 6–17.
- 949 (46) Lookman, T.; Eidenbenz, S.; Alexander, F.; Barnes, C., Eds.;  
950 *Materials Discovery and Design: By Means of Data Science and Optimal  
951 Learning*; Springer International Publishing: Cham, Switzerland, 2018.
- 952 (47) Green, M. L.; Choi, C. L.; Hattrick-Simpers, J. R.; Joshi, A. M.;  
953 Takeuchi, I.; Barron, S. C.; Campo, E.; Chiang, T.; Empedocles, S.;  
954 Gregoire, J. M.; et al. Fulfilling the Promise of the Materials Genome  
955 Initiative with High-Throughput Experimental Methodologies. *Appl.  
956 Phys. Rev.* **2017**, *4*, 011105.
- 957 (48) Woo, S. I.; Kim, K. W.; Cho, H. Y.; Oh, K. S.; Jeon, M. K.;  
958 Tarte, N. H.; Kim, T. S.; Mahmood, A. Current Status of  
959 Combinatorial and High-Throughput Methods for Discovering New  
960 Materials and Catalysts. *QSAR Comb. Sci.* **2005**, *24*, 138–154.
- 961 (49) Koinuma, H.; Takeuchi, I. Combinatorial Solid-State  
962 Chemistry of Inorganic Materials. *Nat. Mater.* **2004**, *3*, 429–438.
- 963 (50) Chen, S.; Hou, Y.; Chen, H.; Tang, X.; Langner, S.; Li, N.;  
964 Stubhan, T.; Levchuk, I.; Gu, E.; Osvet, A.; et al. Exploring the  
965 Stability of Novel Wide Bandgap Perovskites by a Robot Based High  
966 Throughput Approach. *Adv. Energy Mater.* **2018**, *8*, 1701543.
- 967 (51) Xiang, X.-D.; Sun, X.; Briceño, G.; Lou, Y.; Wang, K.-A.;  
968 Chang, H.; Wallace-Freedman, W. G.; Chen, S.-W.; Schultz, P. G. A  
969 Combinatorial Approach to Materials Discovery. *Science* **1995**, *268*,  
970 1738–1740.
- 971 (52) Kirman, J.; Johnston, A.; Kuntz, D. A.; Askerka, M.; Gao, Y.;  
972 Todorović, P.; Ma, D.; Privé, G. G.; Sargent, E. H. Machine-Learning-  
973 Accelerated Perovskite Crystallization. *Matter* **2020**, *2*, 938–947.

- 975 (53) Sun, S.; Hartono, N. T. P.; Ren, Z. D.; Oviedo, F.; Buscemi, A.  
976 M.; Layurova, M.; Chen, D. X.; Ogunfunmi, T.; Thapa, J.; Ramasamy,  
977 S.; Settens, C.; DeCost, B. L.; Kusne, A. G.; Liu, Z.; Tian, S. I. P.;  
978 Peters, I. M.; Correa-Baena, J.-P.; Buonassisi, T. Accelerated  
979 Development of Perovskite-Inspired Materials via High-Throughput  
980 Synthesis and Machine-Learning Diagnosis. *Joule* **2019**, *3*, 1437–  
981 1451.
- 982 (54) MacLeod, B. P.; Parlante, F. G. L.; Morrissey, T. D.; Häse, F.;  
983 Roch, L. M.; Dettelbach, K. E.; Moreira, R.; Yunker, L. P. E.; Rooney,  
984 M. B.; Deeth, J. R.; Lai, V.; Ng, G. J.; Situ, H.; Zhang, R. H.; Elliott,  
985 M. S.; Haley, T. H.; Dvorak, D. J.; Aspuru-Guzik, A.; Hein, J. E.;  
986 Berlinguette, C. P. Self-Driving Laboratory for Accelerated Discovery  
987 of Thin-Film Materials. *Science Advances* **2020**, *6*, eaaz8867.
- 988 (55) Li, J.; Lu, Y.; Xu, Y.; Liu, C.; Tu, Y.; Ye, S.; Liu, H.; Xie, Y.;  
989 Qian, H.; Zhu, X. AIR-Chem: Authentic Intelligent Robotics for  
990 Chemistry. *J. Phys. Chem. A* **2018**, *122*, 9142–9148.
- 991 (56) Lignos, I.; Morad, V.; Shynkarenko, Y.; Bernasconi, C.;  
992 Maceiczyk, R. M.; Protesescu, L.; Bertolotti, F.; Kumar, S.;  
993 Ochsenbein, S. T.; Masciocchi, N.; Guagliardi, A.; Shih, C.-J.;  
994 Bodnarchuk, M. I.; deMello, A. J.; Kovalenko, M. V. Exploration of  
995 Near-Infrared-Emissive Colloidal Multinary Lead Halide Perovskite  
996 Nanocrystals Using an Automated Microfluidic Platform. *ACS Nano*  
997 **2018**, *12*, 5504–5517.
- 998 (57) Lu, S.; Zhou, Q.; Ouyang, Y.; Guo, Y.; Li, Q.; Wang, J.  
999 Accelerated Discovery of Stable Lead-Free Hybrid Organic-Inorganic  
1000 Perovskites via Machine Learning. *Nat. Commun.* **2018**, *9*, 3405.
- 1001 (58) Tabor, D. P.; Roch, L. M.; Saikin, S. K.; Kreisbeck, C.;  
1002 Sheberla, D.; Montoya, J. H.; Dwarakanath, S.; Aykol, M.; Ortiz, C.;  
1003 Tribukait, H.; et al. Accelerating the Discovery of Materials for Clean  
1004 Energy in the Era of Smart Automation. *Nat. Rev. Mater.* **2018**, *3*, 5.
- 1005 (59) Balachandran, P. V.; Kowalski, B.; Sehirioglu, A.; Lookman, T.  
1006 Experimental Search for High-Temperature Ferroelectric Perovskites  
1007 Guided by Two-Step Machine Learning. *Nat. Commun.* **2018**, *9*, 1668.
- 1008 (60) Raccuglia, P.; Elbert, K. C.; Adler, P. D. F.; Falk, C.; Wenny, M.  
1009 B.; Mollo, A.; Zeller, M.; Friedler, S. A.; Schrier, J.; Norquist, A. J.  
1010 Machine-Learning-Assisted Materials Discovery Using Failed Experi-  
1011 ments. *Nature* **2016**, *533*, 73–76.
- 1012 (61) Correa-Baena, J.-P.; Hippalgaonkar, K.; van Duren, J.; Jaffer, S.;  
1013 Chandrasekhar, V. R.; Stevanovic, V.; Wadia, C.; Guha, S.; Buonassisi,  
1014 T. Accelerating Materials Development via Automation, Machine  
1015 Learning, and High-Performance Computing. *Joule* **2018**, *2*, 1410–  
1016 1420.
- 1017 (62) Xu, R. J.; Olshansky, J. H.; Adler, P. D. F.; Huang, Y.; Smith, M.  
1018 D.; Zeller, M.; Schrier, J.; Norquist, A. J. Understanding Structural  
1019 Adaptability: A Reactant Informatics Approach to Experiment Design.  
1020 *Mol. Syst. Des. Eng.* **2018**, *3*, 473–484.
- 1021 (63) Braham, E. J.; Cho, J.; Forlano, K. M.; Watson, D. F.; Arròyave,  
1022 R.; Banerjee, S. Machine Learning-Directed Navigation of Synthetic  
1023 Design Space: A Statistical Learning Approach to Controlling the  
1024 Synthesis of Perovskite Halide Nanoplatelets in the Quantum-  
1025 Confined Regime. *Chem. Mater.* **2019**, *31*, 3281–3292.
- 1026 (64) Pendleton, I. M.; Cattabriga, G.; Li, Z.; Najeeb, M. A.; Friedler,  
1027 S. A.; Norquist, A. J.; Chan, E. M.; Schrier, J. Experiment  
1028 Specification, Capture and Laboratory Automation Technology  
1029 (ESCALATE): A Software Pipeline for Automated Chemical  
1030 Experimentation and Data Management. *MRS Commun.* **2019**, *9*,  
1031 846–859.
- 1032 (65) Brunetti, B.; Cavallo, C.; Ciccioli, A.; Gigli, G.; Latini, A. On  
1033 the Thermal and Thermodynamic (In)Stability of Methylammonium  
1034 Lead Halide Perovskites. *Sci. Rep.* **2016**, *6*, 31896.
- 1035 (66) Fateev, S. A.; Petrov, A. A.; Khrustalev, V. N.; Dorovatovskii, P.  
1036 V.; Zubavichus, Y. V.; Goodilin, E. A.; Tarasov, A. B. Solution  
1037 Processing of Methylammonium Lead Iodide Perovskite from  $\gamma$ -  
1038 Butyrolactone: Crystallization Mediated by Solvation Equilibrium.  
1039 *Chem. Mater.* **2018**, *30*, 5237–5244.
- 1040 (67) Wicker, J. G. P.; Cooper, R. I. Will It Crystallise? Predicting  
1041 Crystallinity of Molecular Materials. *CrystEngComm* **2015**, *17*, 1927–  
1042 1934.
- 68 (68) Shekar, V. et al. Interactive Data Visualization and Analysis 1043 Interface. <https://mybinder.org/v2/gh/darkreactions/rapid/> 1044 master?filepath=RAPID.ipynb (accessed Feb 25, 2020). 1045
- (69) Shekar, V. et al. RAPID Github Repository <https://github.com/darkreactions/rapid> (accessed Apr 23, 2020). 1046
- (70) Nayak, P. K.; Moore, D. T.; Wenger, B.; Nayak, S.; Haghigirad, A. A.; Fineberg, A.; Noel, N. K.; Reid, O. G.; Rumbles, G.; Kukura, P.; et al. Mechanism for Rapid Growth of 1049 Organic-Inorganic Halide Perovskite Crystals. *Nat. Commun.* **2016**, 1051 7, 13303. 1052
- (71) Stoumpos, C. C.; Malliakas, C. D.; Kanatzidis, M. G. 1053 Semiconducting Tin and Lead Iodide Perovskites with Organic 1054 Cations: Phase Transitions, High Mobilities, and Near-Infrared 1055 Photoluminescent Properties. *Inorg. Chem.* **2013**, *52*, 9019–9038. 1056
- (72) Weller, M. T.; Weber, O. J.; Frost, J. M.; Walsh, A. Cubic 1057 Perovskite Structure of Black Formamidinium Lead Iodide,  $\alpha$ - 1058  $[\text{HC}(\text{NH}_2)_2]\text{PbI}_3$ , at 298 K. *J. Phys. Chem. Lett.* **2015**, *6*, 3209–3212. 1059
- (73) Saidaminov, M. I.; Abdelhady, A. L.; Maculan, G.; Bakr, O. M. 1060 Retrograde Solubility of Formamidinium and Methylammonium Lead 1061 Halide Perovskites Enabling Rapid Single Crystal Growth. *Chem.* 1062 **2015**, *51*, 17658–17661. 1063
- (74) Yang, J.; Siempelkamp, B. D.; Liu, D.; Kelly, T. L. Investigation 1064 of  $\text{CH}_3\text{NH}_3\text{PbI}_3$  Degradation Rates and Mechanisms in Controlled 1065 Humidity Environments Using In Situ Techniques. *ACS Nano* **2015**, 1066 9, 1955–1963. 1067
- (75) Frost, J. M.; Butler, K. T.; Brivio, F.; Hendon, C. H.; van 1068 Schilfgaarde, M.; Walsh, A. Atomistic Origins of High-Performance in 1069 Hybrid Halide Perovskite Solar Cells. *Nano Lett.* **2014**, *14*, 2584– 1070 2590. 1071
- (76) Im, J.-H.; Chung, J.; Kim, S.-J.; Park, N.-G. Synthesis, Structure, 1072 and Photovoltaic Property of a Nanocrystalline 2H Perovskite-Type 1073 Novel Sensitizer ( $\text{CH}_3\text{CH}_2\text{NH}_3\text{PbI}_3$ ). *Nanoscale Res. Lett.* **2012**, *7*, 1074 353. 1075
- (77) Safdari, M.; Fischer, A.; Xu, B.; Kloof, L.; Gardner, J. M. 1076 Structure and Function Relationships in Alkylammonium Lead(II) 1077 Iodide Solar Cells. *J. Mater. Chem. A* **2015**, *3*, 9201–9207. 1078
- (78) Stoumpos, C. C.; Cao, D. H.; Clark, D. J.; Young, J.; Rondinelli, 1079 J. M.; Jang, J. I.; Hupp, J. T.; Kanatzidis, M. G. Ruddlesden-Popper 1080 Hybrid Lead Iodide Perovskite 2D Homologous Semiconductors. 1081 *Chem. Mater.* **2016**, *28*, 2852–2867. 1082
- (79) Mitzi, D. B. Synthesis, Crystal Structure, and Optical and 1083 Thermal Properties of  $(\text{C}_4\text{H}_9\text{NH}_3)_2\text{MI}_4$  (M = Ge, Sn, Pb). *Chem.* 1084 *Mater.* **1996**, *8*, 791–800. 1085
- (80) Kim, C.; Huan, T. D.; Krishnan, S.; Ramprasad, R. A Hybrid 1086 Organic-Inorganic Perovskite Dataset. *Sci. Data* **2017**, *4*, 170057. 1087
- (81) Xu, A. F.; Wang, R. T.; Britten, J. F.; Jarvis, V.; Yang, W.; Xu, G. 1088 Pyrrolidinium Lead Iodide from Crystallography: A New Perovskite 1089 with Low Bandgap and Good Water Resistance. *Chem. Commun.* 1090 **2019**, *55*, 3251–3253. 1091
- (82) Kaltzoglou, A.; Stoumpos, C. C.; Kontos, A. G.; Manolis, G. K.; 1092 Papadopoulos, K.; Papadokostaki, K. G.; Pscharis, V.; Tang, C. C.; 1093 Jung, Y.-K.; Walsh, A.; et al. Trimethylsulfonium Lead Triiodide: An 1094 Air-Stable Hybrid Halide Perovskite. *Inorg. Chem.* **2017**, *56*, 6302– 1095 6309. 1096
- (83) Yuan, Z.; Zhou, C.; Tian, Y.; Shu, Y.; Messier, J.; Wang, J. C.; 1097 van de Burgt, L. J.; Kountouriotis, K.; Xin, Y.; Holt, E.; et al. One- 1098 Dimensional Organic Lead Halide Perovskites with Efficient Bluish 1099 White-Light Emission. *Nat. Commun.* **2017**, *8*, 14051. 1100
- (84) Ma, C.; Shen, D.; Huang, B.; Li, X.; Chen, W.-C.; Lo, M.-F.; 1101 Wang, P.; Lam, M. H.-W.; Lu, Y.; Ma, B.; et al. High Performance 1102 Low-Dimensional Perovskite Solar Cells Based on a One Dimensional 1103 Lead Iodide Perovskite. *J. Mater. Chem. A* **2019**, *7*, 8811–8817. 1104
- (85) Seth, C.; Jana, D.; Jindal, V.; Khushalani, D.; Ghosh, S. One- 1105 Dimensional Behavior of Imidazolium Lead Iodide. *J. Phys. Chem. C* 1106 **2019**, *123*, 16449–16455. 1107
- (86) Berg, M.; de Cheong, O.; Kreveld, M.; van Overmars, M. 1108 Computational Geometry: Algorithms and Applications, 3<sup>rd</sup> ed.; 1109 Springer-Verlag: Berlin, 2008. 1110

1111 (87) Aurenhammer, F. Voronoi Diagrams—a Survey of a  
1112 Fundamental Geometric Data Structure. *ACM Comput. Surv.* **1991**,  
1113 23, 345–405.

1114 (88) Travis, W.; Glover, E. N. K.; Bronstein, H.; Scanlon, D. O.;  
1115 Palgrave, R. G. On the Application of the Tolerance Factor to  
1116 Inorganic and Hybrid Halide Perovskites: A Revised System. *Chem.*  
1117 *Sci.* **2016**, 7, 4548–4556.

1118 (89) Jia, X.; Lynch, A.; Huang, Y.; Danielson, M.; Lang'at, I.; Milder,  
1119 A.; Ruby, A. E.; Wang, H.; Friedler, S. A.; Norquist, A. J.; Schrier, J.  
1120 Anthropogenic Biases in Chemical Reaction Data and Their  
1121 Detrimental Effect on Materials Discovery. *Nature* **2019**, 573, 251–  
1122 255.

1123 (90) Wallach, I.; Heifets, A. Most Ligand-Based Classification  
1124 Benchmarks Reward Memorization Rather than Generalization. *J.*  
1125 *Chem. Inf. Model.* **2018**, 58, 916–932.

1126 (91) Pendleton, I. M.; Caucci, M. K.; Tynes, M.; Dharna, A.;  
1127 Nellikkal, M. A. N.; Li, Z.; Chan, E. M.; Norquist, A. J.; Schrier, J. Can  
1128 Machines “Learn” Halide Perovskite Crystal Formation Without  
1129 Accurate Physicochemical Features? *J. Phys. Chem. C* **2020**, in press.

1130 DOI: DOI: [10.1021/acs.jpcc.0c01726](https://doi.org/10.1021/acs.jpcc.0c01726).

1131 (92) Yang, H.; Hamachi, L. S.; Reza, I.; Wang, W.; Chan, E. M.  
1132 Design Rules for One-Step Seeded Growth of Nanocrystals:  
1133 Threading the Needle between Secondary Nucleation and Ripening.  
1134 *Chem. Mater.* **2019**, 31, 4173–4183.